Detection, Classification and Localization of Seabed Objects with a Virtual Time Reversal Mirror

by

Alexis J. Dumortier

M.S. Mechanical Engineering
Georgia Institute of Technology, 2004

Submitted in partial fulfillment of the requirements for the degree of

Master of Science in Oceanographic Engineering

at the

MASSACHUSETTS INSTITUTE OF TECHNOLOGY

and the

WOODS HOLE OCEANOGRAPHIC INSTITUTION

February 2009

Author .....
Joint Program in Oceanography/Applied Ocean Science and Engineering
Massachusetts Institute of Technology
and Woods Hole Oceanographic Institution
September 25, 2008

Certified by .....
Henrik Schmidt
Professor of Mechanical and Ocean Engineering
Thesis Supervisor

Accepted by.....
David Hardt
Chairman, Committee on Graduate Students
Department of Mechanical Engineering
Massachusetts Institute of Technology

Detection, Classification and Localization of Seabed Objects with a Virtual Time Reversal Mirror

by

Alexis J. Dumortier

Submitted to the Department of Mechanical Engineering at the Massachusetts Institute of Technology and the Department of Oceanography/Applied Ocean Science and Engineering at Woods Hole Oceanographic Institute
in September 2008, in Partial Fulfillment of the Requirements for the Degree of Master of Science in Mechanical Engineering

Abstract

The work presented in this thesis addresses the problem of the detection, classification and localization of seabed objects in shallow water environments using a time reversal approach in a bistatic configuration. The waveguide is insonified at low frequency (~kHz) with an ominidirectional source and the resulting scattered field is sampled by a receiving array towed behind an Autonomous Underwater Vehicle (AUV). The recorded signals are then processed to simulate onboard the AUV, the time reversed transmissions which serve to localize the origin of the scattered field on the seabed and estimate the position of the targets present. The clutter rejection based upon the analysis of the singular values of the Time Reversal operator is investigated with simulated data and field measurements collected off the coast of Palmaria (Italy) in January 2008.

Thesis Supervisor: Henrik Schmidt
Title: Professor of Mechanical and Ocean Engineering

Acknowledgments

I would like to express my gratitude to my advisor, Henrik Schmidt for his help, support, and patience throughout the completion of this project. I am also grateful to Karim Sabra for devoting his time and energy to assist me with the processing of the data and for his enthusiasm. I would like to thank Arjuna Balasuriya for his interest in my research work and his encouragements.

This work would not have been possible without the cooperation of the staff of NURC (NATO Undersea Research Center) who provided me with the data of the CCLNet08 sea trial and all the details regarding the experimental setup: David Hughes, Alain Maguer, Marco Mazzi, Alessandro Sapienza, Kevin LePage, Piero Guerrini.

I would also like to thank my friends from the Laboratory of Autonomous Marine Sensing Systems: Kevin Cockrell, Deep Ghosh, Raymond Lum, Maria Parra-Orlandoni, Costas Pelekanakis, Andrew Shafer for their help, their support during difficult times and for having shared with me much more than lab space. I will always be indebted to each of you.

I cannot thank enough my parents and my family for their encouragements, their love and affection.

Contents

List of Figures

Chapter 1

Introduction

1.1 Background and Motivations

Recent developments in Autonomous Underwater Vehicles (AUVs) technology have brought new perspectives in various fields of ocean engineering such as oil exploration, fishery, marine archeology and mine countermeasures (MCMs). The deployment of autonomous vehicles requires significantly less manpower than surface vessels and is often better adapted to exploring areas with limited access. For economic reasons, the choice of inexpensive platforms to collect data also presents competitive advantages for many applications. The costs involved in mine hunting missions conducted from military ships are reduced by using AUVs which also allow for safer, cooperative and inexpensive operations. However, the shift toward smaller platforms for MCMs as well as for many other fields also introduces new challenges, each of which calls for innovative solutions.

Power limitations onboard AUVs impose reduced power-budgets allowable for the processes running on the payload and call for efficient algorithms. The efficiency of active Detection Localization and Classification (DCL) techniques in the field of MCM can be measured in terms of coverage rates and false alarm rates. Coverage rates are typically constrained by the frequency band of the detection signals. High frequencies ($\sim$MHz) used by side-scan sonars provide high-resolution images of the seafloor at the cost of limited coverage rates due to the high attenuation associated with short wavelengths in seawa-

ter. In addition, the poor bottom penetration of high frequency signals also prevents their use for the detection of mines buried in the seabed. In comparison, low-frequency signals ($\sim$kHz) suffer little transmission losses, penetrate deeper into the seabed and can reveal the structural response of mine-like elastic objects [1]. The scattering from elastic spherical shells at low-frequency has been investigated during past experiments [2] [3] along with the development of high-fidelity numerical models that can now treat a broad class of scattering problems [4] [5]. The sampling of low-frequency scattered fields using AUVs has long been problematic due to the lack of control techniques adapted to the towing of long receiving antennas by a small platform. A behavior-based control approach [6] recently tested at sea with a 100m long array towed behind a 21 inch AUV demonstrated robust control maneuvers and brings promising sensing capabilities for AUVs.

The presence of multipath and reverberation in shallow waveguides greatly complicates the detection of target echoes and constitute a limiting factor for most DCL techniques. Therefore, the focusing of acoustic energy on potential targets is desirable in order to achieve higher signal to noise ratio. In homogeneous and unbounded media, focusing monochromatic signals in space can be achieved with a set of acoustic sources by properly choosing their amplitude and relative phase delays. Beamforming techniques are commonly used to estimate this weighting from geometrical approximations and produce with an array of sources, a set of pressure wave-fronts that interfere constructively in the focusing region. In ocean waveguides, however, the task of estimating appropriate amplitude and phase delays that account for boundary reflections becomes intractable without the knowledge of the environment. In contrast, the Time Reversal (TR) process automatically determines the response of the waveguide from the scattered field measurements to compensate for multipath effects. The ability of the TR acoustics methods to achieve focusing in time and space without prior knowledge of the environment has attracted a lot of attention among acousticians [7] [8] [9] [10]. Focusing techniques based upon the TR process have been developed to handle multiple scatterers and extract simultaneously the location and classification information about each target with minimal computation effort [11].

1.2 Thesis objectives

The main objective of this research is to investigate the concurrent detection classification and localization of seabed objects using a TR approach. The DCL technique involves a single acoustic source and a set of receivers in a bistatic configuration. The source insonifies the target field at low frequency while the scattered field is sampled with a receiving array towed behind an AUV. The detection of the scatterers requires the analysis of invariants of the TR process determined from the singular value decomposition of the TR operator. The localization of the scatterers is then achieved with a Time Reversal imaging of the seabed, best described as a "virtual" TR mirror since it does not imply actual acoustic transmissions. Due to the limited amount of calculations involved in the detection and localization process, this approach is well suited to AUV operations. In order to meet our objective, we consider the following intermediary steps:

- Modeling of realistic operational scenarios to test the feasibility of the virtual TR mirror approach and understand its limitations
- Implementation of the TR imaging used to localize the seabed targets
- Testing of the virtual TR mirror approach with experimental data

1.3 Thesis Outline

The thesis report will be organized as follows:

The second chapter introduces the theoretical concepts upon which the proposed approach is based. In particular, the derivation of several focusing methods is presented to formulate the relations between the eigenstates of the TR process and the scatterers present. The theory on scattering from elastic spherical shells is also reviewed. The chapter concludes with the review of past research work in the field of Time Reversal acoustics.

The third chapter describes the modules involved in the modeling of the broadband insonification of a shallow water waveguide in presence of targets located on the seabed and the measurement of the resulting scattered field at the receiving array. It also provides justifications for the modeling simplifications made to reduce computation time while maintaining modeling accuracy. Finally, the principle of the virtual Time Reversal mirror used localize the scatterers on the seabed is presented along with the analysis of simulated results.

The fourth chapter presents the setup of the sea trial that took place near the island of Palmaria (Italy) in January 2008 and the steps taken to process our experimental data. In particular the time of arrival of echoes from the scatterers are determined from the analysis of the singular value of the TR operator and compared to the time of arrival estimated using geometrical consideration. The localization of the scatterers based upon the virtual time reversal mirror approach is also compared to known positions of the scatterers present.

The last chapter concludes the thesis and summarizes the simulated and experimental results. In light of observations made, several limitations of the proposed approach are presented along with possible future developments.

Chapter 2

Theoretical Background

This chapter introduces the theoretical concepts underlying the virtual TR mirror approach presented in the third chapter of the thesis and reviews past research work in the field of Time Reversal Acoustics.

2.1 Time Reversal Acoustics

2.1.1 Background

The wave equation governing the propagation of pressure waves in lossless inhomogeneous media is given by:

$$\rho(r)\nabla \cdot \left(\frac{1}{\rho(r)}\,\nabla p\right) - \frac{1}{c^2(r)}\,\frac{\partial^2 p}{\partial t^2} = 0 \tag{2.1}$$

where p, c, and ρ refer respectively to the pressure, sound speed and density in the medium.

Since the order of the time derivative in Eq. (2.1) is even, if a function $p(r,t)$ satisfies the wave equation, its time reversed form, $p(r,-t)$ is also a solution of the wave equation. From a practical aspect, the invariance of the wave equation to time inversion implies that the field emitted from a source can be recorded, time reversed and focused back at the source location as if time was running backwards. Achieving time reversed focusing

requires that time shift invariance, linearity and reciprocity hold in the environment.

Time Reversal mirrors (TR mirrors) are physical implementations of the time reversal procedure. The TR mirror typically consists of a set of receivers connected to a storage device that records the pressure field incident on the mirror. A set of sources co-located with the receivers of the TR mirror retransmits the recorded signals in a time reversed manner (First In Last Out). During the backpropagation, the acoustic field produced by each source of the TR mirror interferes constructively where the pressure field initially measured by the TR mirror was emitted and destructively elsewhere. TR mirrors are well suited for active detection purpose since they allow to focus energy on reflective scatterers playing the role of sources after insonification of the environment.

2.1.2 Time Reversal process

We describe in more details the steps involved in a focusing cycle in presence of a single scatterer in a free field environment. The sources of the TR mirror first insonify the environment with a set of probing signals $e_m(t)$ ($m = 1, ..., N$ assuming N sources) (Fig. 2-1).

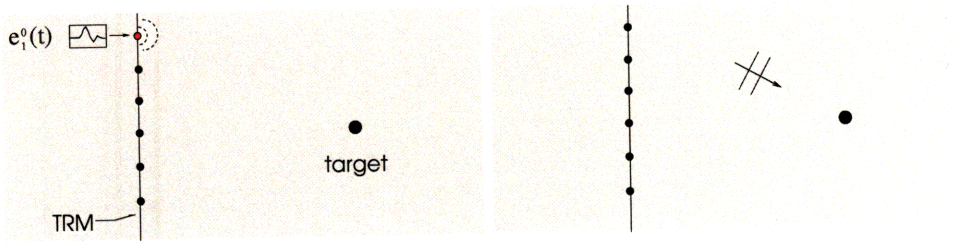

Figure 2-1: Target Insonification

The resulting scattered field measured at the l^{th} receiver of the TR mirror ($l = 1, ..N$) (Fig. 2.2(a)) is expressed as follows:

$$r_l(t) = \sum_{m=1}^{N} k_{lm}(t) \otimes e_m(t) \tag{2.2}$$

where $k_{lm}(t)$ is the impulse response between element m and element l of the TR mirror. "$\otimes$" denotes the time domain convolution. In the frequency domain, Eq. (2.2) becomes:

$$R_l^0(\omega) = \sum_{m=1}^{N} K_{lm}(\omega) E_m^0(\omega) \tag{2.3}$$

where the 0 index refers to the initial cycle.

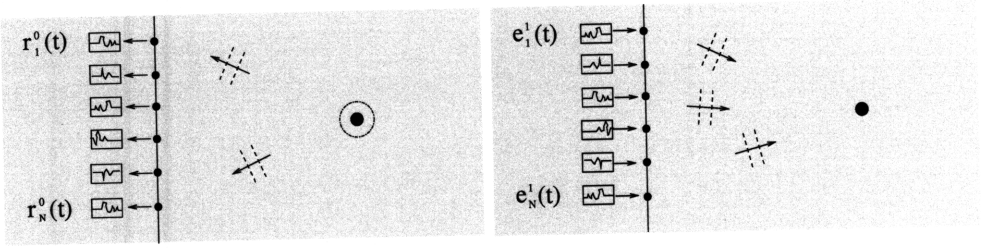

(a) (b)

Figure 2-2: Backpropagation in presence of a single scatterer

The field recorded at the receivers is then time reversed or equivalently phase conjugated in the frequency domain. The new set of signals to be transmitted (Fig. 2.2(b)) in order to focus on the target is expressed as:

$$E_l^1(\omega) = \sum_{m=1}^{N} K_{lm}^*(\omega) E_m^{0*}(\omega) \tag{2.4}$$

or in matrix notation:

$$E^1(\omega) = K^*(\omega) E^{0*}(\omega) \tag{2.5}$$

where $K(\omega)$ refers to the interelement matrix evaluated at the frequency ω.

In presence of a single scatterer, repeating the focusing cycles progressively reduces the extent of the focusing region and converges to an optimized set of amplitudes and phase delays associated with the scatterer. The analysis of convergence of successive focusing

cycles in presence of multiple scatterers yields the iterative focusing approach.

2.1.3 Iterative Focusing Approach

In presence of multiple reflectors, the procedure described in section 2.1.2 is repeated in order to focus on the most reflective scatterer by iteratively filtering the scattered field of weaker reflectors. This self-converging process initially formulated by C.Prada [12] yields without calculations the amplitudes and phase delays that are to be applied to the sources of the TR mirror in order to achieve focusing on the dominant scatterer. We proceed with an analysis of convergence of the iterative focusing approach in presence of a set of d point-like scatterers (where $d < N$) with distinct reflectivities.

The focusing procedure introduced in section 2.1.2 yields the signals to be transmitted by the TR mirror in order to focus on the scatterer present. The same approach applies in presence of multiple well-resolved[1] scatterers and results in a transmitted field that initially focuses on each of them. Starting from Eq. (2.5), the scattered field resulting from the transmission of $E^1(\omega)$ by the TR mirror is given by:

$$R^1(\omega) = K(\omega)E^1(\omega) \tag{2.6}$$

and yields the transmitted signal of the next cycle:

$$E^2(\omega) = R^{1*}(\omega) \tag{2.7}$$

$$= [K^*(\omega)K(\omega)]E^0(\omega) \tag{2.8}$$

$K^*(\omega)K(\omega)$ in Eq. (2.8) is referred to as the Time Reversal operator (TR operator). Since reciprocity holds in the environment, the interelement matrix K is symmetric and consequently the TR operator matrix is hermitian, has real positive eigenvalues and orthogonal eigenvectors. In presence of point-like well-resolved isotropic scatterers, the rank of

[1] Scatterers are said to be well-resolved when the field focused on one of them does not insonify the other scatterers present

the TR operator is equal to the number of reflectors present [13] and each eigenvalue $\lambda_i(\omega)$ (i=1,...,d) (and corresponding eigenspace) is associated with one of the reflectors present. Therefore, any vector can be expressed as a combination of d non-null vectors from these eigenspaces. For example, the first transmission vector $E^0(\omega)$ can be expressed as:

$$E^0(\omega) = F_1(\omega) + F_2(\omega) + ... + F_d(\omega) \tag{2.9}$$

where $F_i(\omega)$ is a vector from the i^{th} eigenspace. Using this form of $E^0(\omega)$, the transmitted signals corresponding to the $2n$ iteration and given by:

$$E^{2n}(\omega) = [K^*(\omega)K(\omega)]^n E^0(\omega) \tag{2.10}$$

can be rewritten as:

$$E^{2n}(\omega) = \lambda_1^n(\omega)F_1(\omega) + \lambda_2^n(\omega)F_2(\omega) + ... + \lambda_d^n(\omega)F_d(\omega) \tag{2.11}$$

Similarly the transmitted signals corresponding to the $2n+1$ iteration expressed as:

$$E^{2n+1}(\omega) = [K^*(\omega)K(\omega)]^n K^*(\omega)E^{0*}(\omega) \tag{2.12}$$

can be rewritten as:

$$E^{2n+1}(\omega) = \lambda_1^n(\omega)K^*(\omega)F_1^*(\omega) + ... + \lambda_d^n(\omega)K^*(\omega)F_d^*(\omega) \tag{2.13}$$

For a large number of iterations, Eq. (2.11) and Eq. (2.13) converge respectively as follow:

$$E^{2n}(\omega) \approx \lambda_j^n(\omega)F_j(\omega) \qquad E^{2n+1}(\omega) \approx \lambda_j^n(\omega)K^*(\omega)F_j^*(\omega) \tag{2.14}$$

where j is the index associated with the largest eigenvalue of the TR operator. Eq. 2.14 shows two distinct limits of convergence of the iterative approach both associated with the dominant scatterer. The DORT method described in the section 2.1.4 extends this analysis

to the remaining eigenvectors of the TR operator to achieve selective focusing on the each scatterer present.

2.1.4 DORT Method

The DORT[2] method enables selective focusing in a multiple-scatterer environment. The technique consists of the following steps:

1. Construction of the interelement matrix $K(\omega)$,
2. Extraction of the eigenvalues and eigenvectors of the TR operator $(= K^*(\omega)K(\omega))$,
3. Focusing on a selected scatterer by transmission of its associated eigenvector.

The formulation of the DORT method is a direct consequence of the convergence analysis of the iterative focusing approach. It was demonstrated in section 2.1.3 that the iterative approach yields the focusing on the strongest scatterer present. The following derivations show that in the presence of point-like well-resolved isotropic scatterers of different reflectivity, the transmission of each eigenvector of the TR operator allows for the focusing on its associated scatterer.

Considering the transmission of an impulse signal $\delta(t)$ from the location of the i^{th} scatterer present, the field measured at the TR mirror by the l^{th} receiver is expressed as $a_r(t) \otimes h_{il}(t)$ where $a_r(t)$ is the acoustoelectrical response in reception of the receivers of the TR mirror. For simplicity the receivers of the array are assumed to have identical response in reception. $h_{il}(t)$ referes to the diffraction impulse response between the i^{th} scatterer and the l^{th} receiver of the TR mirror. The field to be emitted by the l^{th} source of the TR mirror in order to focus at the location of the i^{th} scatterer is given by $a_r(-t) \otimes h_{il}(-t)$ and the pressure field at the location of the j^{th} scatterer after the time reversed transmission is expressed as:

$$P_j(\omega) = A_r^*(\omega)A_e(\omega)\sum_{l=1}^{N} H_{jl}(\omega)H_{il}^*(\omega) \tag{2.15}$$

[2]French acronym for "Décomposition de l'Opérateur de Retournement Temporel"

The term $A_e(\omega)$ in Eq. (2.15) refers to the Fourier transform of the response in emission of the sources of the TR mirror. For simplicity the sources of the array are assumed to have identical response in emission.

In a vector form Eq. (2.15) becomes:

$$P(\omega) = A_r^*(\omega)A_e(\omega)^T H_j(\omega)H_i^*(\omega) \tag{2.16}$$

The condition of well-resolved scatterers implies that the vectors $H_i(\omega)$ are orthogonal and that the field produced at the j^{th} reflector and given by equation (2.16) is null unless $i = j$. The preceding analysis demonstrates that propagating $H_i^*(\omega)$ from the TR mirror allows to focus on the i^{th} reflector present. We now show that $H_i^*(\omega)$ is the eigenvector of the TR operator associated with the eigenvalue $\lambda_i(\omega)$. Transmitting $H_i^*(\omega)$ from the TR mirror produces a scattered field measured at the TR mirror and given by $K(\omega)H_i^*(\omega)$. The component of the scattered field measured at the receiver l is expressed as:

$$R_l(\omega) = \sum_{m=1}^{N} H_{im}^*(\omega)K_{ml}(\omega) \tag{2.17}$$

Introducing the reflectivity of each scatterer $C_1(\omega)$, $C_2(\omega)$,...,$C_d(\omega)$, the interelement frequency response $K_{ml}(\omega)$ can be related to the diffraction response as follows:

$$K_{ml}(\omega) = \sum_{k=1}^{d} H_{mk}(\omega)C_k(\omega)H_{kl}(\omega) \tag{2.18}$$

Using the fact that the diffraction responses are orthogonal, Eq. (2.17) becomes:

$$R_l(\omega) = H_{il}(\omega)C_i(\omega)\sum_{m=1}^{N} |H_{im}(\omega)|^2 \tag{2.19}$$

or in a vector form:

$$K(\omega)H_i^*(\omega) = C_i(\omega)\sum_{m=1}^{N} |H_{im}(\omega)|^2 H_i(\omega) \tag{2.20}$$

Finally multiplying Eq. (2.20) by $K^*(\omega)$ and replacing $K(\omega)^* H_i(\omega)$ by its form in Eq. (2.20) yields:

$$K^*(\omega)K(\omega)H_i^*(\omega) = |C_i(\omega)|^2 \left(\sum_{m=1}^{N} |H_{im}(\omega)|^2 \right)^2 H_i^*(\omega) \tag{2.21}$$

From Eq. (2.21), it is clear that the eigenvector $H_i^*(\omega)$ of the TR operator is associated with the eigenvalue $\lambda_i(\omega)$ defined as :

$$\lambda_i(\omega) = |C_i(\omega)|^2 \left(\sum_{m=1}^{N} |H_{im}(\omega)|^2 \right)^2 \tag{2.22}$$

Thus the magnitude of each eigenvalue is equal to the square of the effective reflectivity of the corresponding reflector. It is important at this point to make the distinction between the effective reflectivity of the scatterer and its structural reflectivity. The form of $\lambda_i(\omega)$ shows that the effective reflectivity of a scatterer depends on the coefficient of reflexion but also on the transmission between the scatterer and the receivers of the TR mirror.

The iterative focusing approach generates a vector field that converges to the eigenvector produced by the DORT method for the dominant scatterer. However in presence of scatterers with similar effective reflectivities, the convergence process requires a large number of iterations. Furthermore, it does not provide any of the eigenvectors associated to the weaker scatterers present. In these regards, the DORT method overcomes the limitations of the iterative focusing approach but does so at the cost of the time consuming construction of the TR operator which is not needed by the iterative approach. The interelement response $k_{lm}(t)$ between element l and element m is measured by emitting an impulse from the source l of the TR mirror and recording the scattered field at the receiver m. Due to the reciprocity of the transmission, $k_{lm}(t) = k_{ml}(t)$ and for a TR mirror of N element the construction of the TR operator requires $N^2/2$ measurements. An alternative approach well suited to reverberating waveguides has been introduced by Lingevitch [14] and results in higher signal to noise ratios during waveguide insonification. A set of beams defined by orthogonal weighting vectors at the transmitting array is used to insonify the

waveguide in place of the conventional insonification from individual sources. The process results in a "beam space" interelement response matrix from which the "element space" interelement response is recovered with a simple matrix manipulation.

2.1.5 Covariance matrix representation of the TR operator

In section 2.1.3 and 2.1.4, the construction of the TR operator is formulated for a set of stationary co-located sources and receivers. The virtual TR mirror approach presented in this thesis however involves a moving source that insonifies the waveguide at regular time intervals and a receiving array towed behind an AUV (Fig 4-1).

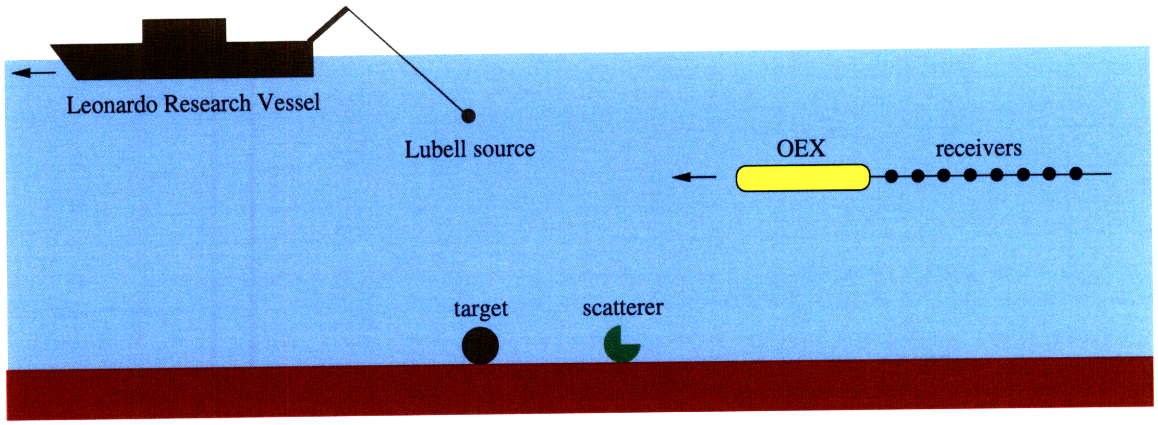

Figure 2-3: Bistatic configuration envisioned for the virtual TR mirror approach

Here, the condition of a stationary array is re-created by restricting our processing to a set of receivers that overlap at the time of emissions of the source. In the configuration described here, Doppler shifts are introduced due to the relative motion between the source and the targets and due to the motion of the receivers relative to the target. However, since the waveguide is insonified at low frequency and since the speed of the source of the receivers is small Doppler effects are assumed to be negligible. Therefore the source is considered stationary at each time of emission and it re-creates from its successive positions a stationary transmitting array (Fig 2-4).

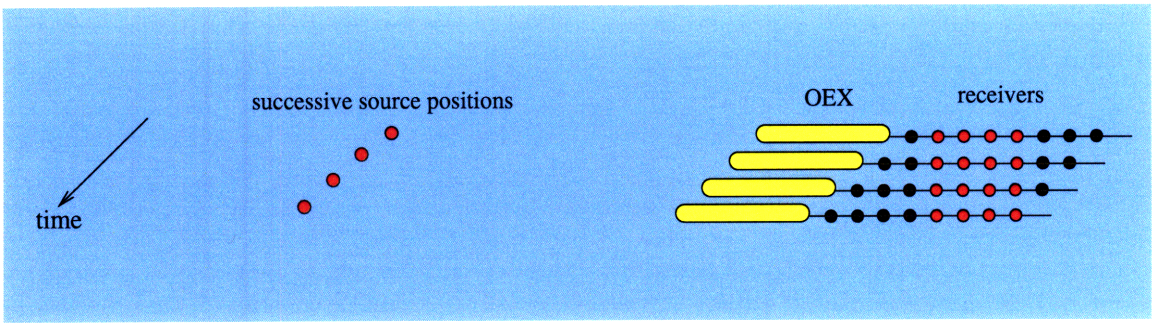

Figure 2-4: Set of receivers chosen for the construction of the TR operator

For configurations that involve separated array of sources and receivers, invariants of transmissions of the TR process are identified with a similar approach as described in section 2.1.3: the interelement matrix K is constructed by measuring the field incident on a stationary receiving array subsequent to successive emissions of probing signals from each source of the transmitting array [8]. The Singular Value Decomposition of the interelement matrix (or equivalent eigenvalue decomposition of the $TRO = K^*K^T$) provides each eigenstate of the TR process. This form of the TR operator that differs from the previously introduced K^*K, allows to obtain a Hermitian matrix from non-symmetric interelement matrix [15] which is particularly useful in channels where the short time coherence affects the reciprocity. Our approach to construct the TR operator (in the form K^*K^T) involves a passive source detection technique based on the decomposition of the covariance matrix. We present below some of the steps of the construction of the covariance matrix described in [10] [16] [17].

Assuming a linear time-invariant environment where d sources emit the signals $s_1(t)$,..., $s_d(t)$ measured by L receivers. The signal measured at receiver l is given by:

$$r_l(t) = \sum_{i=1}^{d} h_{li}(t) \otimes s_i(t) + b(t) \tag{2.23}$$

where $h_{li}(t)$ refers to the impulse response from the source i to the receiver l. $b(t)$ refers to the noise signal measured at the receiver. In the frequency domain, Eq. (2.23) yields the following matrix formulation:

$$R(\omega) = \mathbf{H}(\omega)S(\omega) + B(\omega) \tag{2.24}$$

where $\mathbf{H}(\omega)$ is the transfer matrix from the sources to the receivers and $B(\omega)$ is the noise vector. Each of the M realizations is associated with the column vector $R_m(\omega)$ of the received signal. An estimate of the covariance matrix is obtained from :

$$C(\omega) = \sum_m R_m(\omega)^T R_m(\omega)^* \tag{2.25}$$

Assuming that the background noise and the sources are mutually decorrelated, the covariance matrix is expressed as:

$$\langle \mathbf{C}(\omega) \rangle = \mathbf{H}(\omega)\langle S(\omega)^T S(\omega)^* \rangle^T \mathbf{H}(\omega)^* + \langle B(\omega)^T B(\omega)^* \rangle \tag{2.26}$$

The assumption of uncorrelated sources yields:

$$\mathbf{H}(\omega)\langle S(\omega)^T S(\omega)^* \rangle^T \mathbf{H}(\omega)^* = \langle |S(\omega)|^2 \rangle \mathbf{H}(\omega)^T \mathbf{H}(\omega)^* \tag{2.27}$$

Also assuming an incoherent background noise yields:

$$\langle B(\omega)^T B(\omega)^* \rangle = \sigma^2 \mathbf{I} \tag{2.28}$$

Combining Eq. (2.26), Eq. (2.29) and Eq. (2.28), the diagonalization of the covariance matrix is given by:

$$\lambda_i = \langle |S_i(\omega)|^2 \rangle \sum_{l=1}^{L} |H_{il}(\omega)|^2 + \sigma^2 \tag{2.29}$$

For the implementation of the virtual TR mirror approach, the TR operator is constructed from the estimated covariance matrix given in Eq. (2.25). The sum over several source realizations allows to average out the noise contribution in the measured signals.

2.2 Scattering from elastic targets

The classification of seabed objects as "elastic target" or "clutter" relies on the comparison of their response subsequent to an incident acoustic field. In the context of the DORT method, the singular value decomposition of the TR operator constructed from successive scattered field measurements provides classification information for each target present. However understanding the characteristics of the scattered fields associated with objects of different nature is essential to implement a reliable classification procedure based on the resulting singular values. In this section, the scattering from elastic spherical shells subsequent to a plane wave insonification is introduced with an emphasis on the differences between the scattering from rigid (i.e high density contrast) and elastic objects.

The Resonance Scattering Theory originally introduced in quantum mechanics and first applied to classical physics by Flax [18] has been used to investigate various acoustic scattering problems involving elastic objects. The formulation of scattering problems with the Resonance Scattering Theory underlines the physical meaning of each component of the scattered field and their angular dependence. The scattering from cylinders and spheres has been studied based upon this approach. We examine in this section the scattering in free field resulting from a plane wave incident on a spherical shell. A complete analysis of the scattered field from elastic spherical shells based upon the resonance scattering theory has previously been reported [19] and [20]. Here, we present several of the steps of the derivation presented in [20] along with properties of the elastic waves given in [1].

Given a plane wave insonification of amplitude p_0 expressed as:

$$p_i = p_0 \exp[i(kr - \omega t)] \tag{2.30}$$

The scattered field from an elastic spherical shell takes the form:

$$p_s = p_0 \exp[-i\omega t] \sum_{n=0}^{\infty} i^n (2n+1) R_n h_n^{(1)}(kr) P_n(\cos(\theta)) \tag{2.31}$$

where R_n is a function of the wavenumber k of the incident plane wave and a the outer radius of the spherical shell which involves the density and phase speed of the shell material and surrounding medium. r is the radial distance from the center of the shell, n is the modal order, $h_n^{(1)}$ is the spherical Hankel function of the nth order and P_n is the Legendre polynomial of the nth order. The partial-wave scattering function S_n and the scattering phase shift δ_n are related as follows:

$$S_n = 2R_n + 1 \equiv \exp(2i\delta_n) \tag{2.32}$$

Introducing the form function $f(\theta)$ expressed as a sum of partial waves functions

$$f(\theta) = \sum_{n=0}^{\infty} f_n(\theta) \tag{2.33}$$

$$f_n(\theta) = \frac{2}{ka}(2n+1)S_n^{1/2}\sin\delta_n P_n(\cos(\theta)) \tag{2.34}$$

and the asymptotic representation of the spherical Hankel function

$$h_n^{(1)}(kr) \sim \frac{1}{kr} i^{-(n+1)} \exp(ikr) \tag{2.35}$$

The scattered field in the limit $r \to \infty$ takes the form

$$p_s \sim p_0 \frac{a}{2r} \exp[i(kr - \omega t)] f(\theta) \tag{2.36}$$

The scattering from elastic objects can be represented as the superposition of a rigid body contribution and a radiation contribution. For thin spherical void elastic shells, the radiation contribution at low-frequency (i.e for small values of ka) is limited to the lowest order compressional and flexural modes and their respective circumferential Lamb-type waves: the symmetric wave S_0 and antisymmetric wave A_0. Upon fluid loading, the antisymmetric wave A_0 bifurcates into two dispersive waves A_{0^-} and A_{0^+}. The symmetric S_0 wave is supersonic and reradiates periodically out of the spherical shell at the coupling angle defined as follow:

$$\theta_c = \arcsin\left(\frac{c_{ext}}{c_{shell}}\right) \tag{2.37}$$

where c_{ext} refers to the sound speed of the surrounding medium and c_{shell} refers to the phase speed of the S_0 wave in the shell. Fig. 2-5 depicts the travel paths of the A_0- and S_0 Lamb-type elastic waves backscattered by a spherical shell after insonification around the coincidence frequency. The radiation angles are outlined for the two wave types.

At higher frequencies, the amplitude of the response of the elastic target increases within the mid-frequency enhancement region where the phase speed of the A_0- wave approaches that of the surrounding medium and reaches a maximum at the coincidence frequency f_c defined as:

$$f_c \approx \frac{c_{ext}}{2\pi d} \tag{2.38}$$

where d defines the shell thickness. From the measurement of the time of arrival of the S_0 reradiated waves, Eq. (2.38) can be used to estimate the shell thickness. As the frequency increases above the mid-frequency enhancement region the number of modes excited increases.

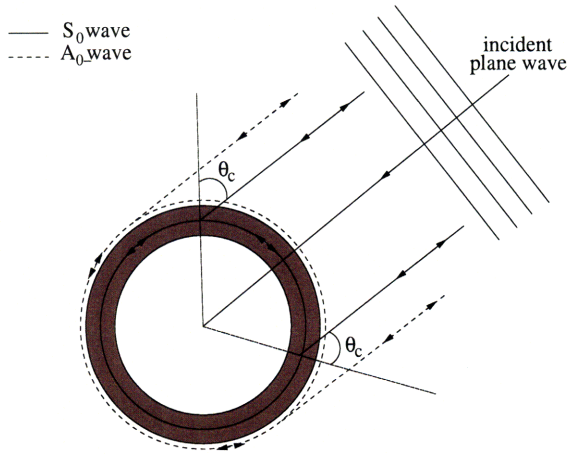

Figure 2-5: Scattering from a spherical shell subsequent to a plane wave insonification

The dissipation of the circumferential waves determines the number of reradiation detectable and consequently the duration of the elastic response. The scattering from rigid objects defined by large density contrast with the surrounding medium, differs from that of elastic objects in that the radiation contribution is negligible and the scattered field reduces to the specular echo of the incident field. From the perspective of the TR operator, the presence of the elastic response in the scattered field introduces new invariants of transmission and therefore additional eigenstates of the TR process associated with the modes of the target. As a result, for similar configuration and target size, the number of significant singular values associated with an elastic target is expected to be larger. In a waveguide, the number of singular values associated with an object also depends on the presence of boundaries that introduce its images and therefore virtually extends its size.

2.3 Literature review

2.3.1 Iterative Focusing Approach

In 1989, Fink extended the phase conjugation method - used in optics to correct the wavefront distortion affecting monochromatic signals - to broadband signals with the formulation of the Time Reversal Mirror [21]. The time reversal process was first applied to the problem of focusing through aberrating media in pulse echo mode and to selective focusing in presence of multiple scatterers. Numerical simulations of the iterative focusing approach were presented in 1991 [22] to examine the effect of the array aperture and of the difference of reflectivities between scatterers. In 1995, the convergence of the iterative focusing method was investigated for well and poorly resolved scatterers [12]. The theoretical analysis showed distinct limits of convergence for odd and even number of iterations. The number of iterations needed to achieve convergence on the dominant scatterer was found to depend on the differences of reflectivity between the scatterers. The iterative focusing approach was explored at sea in 1999 [23] with a TR mirror spanning the water column and a receiving array located at the focusing range. A probe source was used in place of a scatterer to insure higher signal to noise ratios and the field transmitted by the TR mirror

after each iteration was amplified. A spread in time of the signal measured at the retrofocus location was attributed to the bandpass filtering introduced by the transducers of the TR mirror and the waveguide. In 2004, Montaldo [24] proposed a solution to the problem of time spreading. The method based on the iterative focusing approach resolves the wavefronts associated with each scatterers from the signals measured at the TR mirror. Each set of wavefronts detected is then recompressed in time prior to its retransmission to limit the bandpass filtering introduced by the transducers of the TR mirror and the waveguide. The same authors [25] introduced a new method based on the iterative focusing approach that involves two Source Receivers Arrays (SRA). A control array measures the field produced by the emitting array and compares it to a objective/desired field at the control array. The difference between the desired field and the measured field at the control array is then used to adjust iteratively the field transmitted from the emitting array and successively achieve optimum focusing. This technique overcomes the time spreading effects mentioned earlier and allows to achieve optimum focusing faster and with little computation efforts.

2.3.2 DORT method

In order to provide the reader with an organized literature review of the DORT method, the following section is divided into categories of problems to which the DORT method has been applied. Within each category, the publications are presented in chronological order.

Selective focusing on point-like and extended scatterers

In 1993, the theoretical formulation of the DORT method was introduced from the derivation of the iterative focusing approach [26] and the predictions made with the method were confirmed by simulated results [11]. The selective focusing based on the DORT method was investigated theoretically for well-resolved wires and the focusing ability of the DORT method was compared to that of the iterative approach for the most reflective scatterer of a set. Experimental results showed that both methods have the same ability to focus in space however the DORT method achieves focusing with only one iteration. Prada extended the DORT method to a finite size hollow cylinder and found that each eigenstate of the TR

operator is associated with a circumferential elastic wave and two points of emission on the cylinder [27]. The experimental backpropagation of each eigenvector confirmed this analysis and allowed an accurate estimation of the phase speed associated with each type of wave. In 1996, the special case of selective focusing on two targets with same apparent reflectivities was investigated theoretically and experimentally [7]. In such configuration, the DORT method produces two eigenvectors with unique characteristics. The magnitude of the first eigenvector shows in-phase contributions of the two targets while the second eigenvector shows their out-of-phase contributions. Selective focusing in this case requires the backpropagation of a linear combination of the two eigenvectors. In light of these results, the scattering analysis from the hollow cylinder conducted in 1994 was revisited [28]. The two secondary sources (associated with the radiation of elastic waves) have identical "reflectivities" and as observed for the two well resolved wires, the DORT method results in two eigenvectors whose magnitude exhibit interferences of these secondary sources radiating in-phase and out-of-phase. In 2001, Chambers carried out the theoretical analysis of the time reversal process associated with a homogeneous point-like scatterers (i.e. subwavelength and spherical) and demonstrated that one eigenstate of the TR operator is associated with the compressibility contrast between the scatterer and the medium while three other eigenstates are associated with the density contrast [13]. The analysis of the TR operator conducted on subwavelength isotropic and anisotropic cylinders results in observations validated by ultrasonic experiments [29]. Chambers applied the theoretical analysis of the DORT method to finite objects of simple geometry such as spheres and finite objects of arbitrary geometry in far-field configurations and confirmed theoretically the relation between the number of eigenvalues associated with an extended scatterer and its size [30]. Minonzio investigated the relation between the modes of vibrations of an elastic scatterers (caused by the density and compressibility contrasts), the projected harmonics associated with each mode and the singular values of the TR operator [31]. In particular, the maximum number of projected harmonics resolvable by the receiving array yields the possible reduction of the dimension of the TR operator.

Environment effects on selective focusing

In 1995, the selective focusing method was tested with a layer of inhomogeneous aberrating media separating the TR mirror from the scatterers [32]. It was shown experimentally that selective focusing on well-resolved scatterers can be achieved under the condition that the phase variations introduced by the layer of aberrating medium are smooth. In 1999, Mordant showed significant improvements in resolution obtained when focusing in a waveguide. Each image of the TR mirror relative to the waveguide boundaries virtually increases its extent and allows for higher resolution focusing compared to predicted resolution in free field. The effects of time variance of the environment on the selective focusing were investigated experimentally in presence of waves of varying amplitude [9]. It was observed that increasing the wave amplitudes increases the amplitude of the noise eigenvalues and decreases the amplitude of the eigenvalues associated with the targets. Finally, Mordant formulated the condition for selective focusing in time and space. The time domain DORT method requires that the reflectivity of each scatterers present in the waveguide allows to attribute to each of them the corresponding eigenvector over the frequency band of a short duration pulse. A similar study from Roux [33] also provided an analysis of the temporal focusing in the waveguide and general formulations for the size of the focal spot and sidelobe levels around the focal spot. In particular, it was observed that the size of the retrofocus increases when the insonifying source is located near the interface. Sabra and Dowling reported on the effect of background noise [34], array motion [35], array deformation [36] and ocean currents [37] on retrofocusing in shallow water environments providing theoretical background for realistic time reversal scenarios in ocean waveguides. The effect of bottom absorption and reverberation on the resolution of the focusing have been investigated [38] and a method was presented to compensate for transmission losses affecting each multipath between the TR mirror and the scatterer and improve signal to noise ratio at the scatterer but requires prior knowledge of the environment. In the light of earlier investigations showing degraded retrofocus in reverberating environments, several solution were proposed that attempt to reduce the amount of backpropagated field reaching the seabed at the focusing range. Kim [39] discussed the potential benefits of using a prob-

ing source located at mid-depth to determine the field to be transmitted by the TR mirror in order to produce a null of transmission near the bottom at the range of the probing source. A similar approach consisted in insonifying a mid-depth target with a probing source and showed improvements in the backpropagated field reaching the target. The use of a probing source however limited the potential of these approaches. Instead, simulated results from Song [40] explored the possibility of determining the eigenvector associated with the seabed reverberation at a range of desired focusing to generate a nulling vector by linearly combining the remaining orthogonal eigenvectors of the TRO. [41]

Time Reversal Imaging

The localization and shape estimation of extended targets based on TR imaging has been investigated in publications related to inverse problems. In 2004, Hou layed out an approach based upon the coupling of the target location estimation with a shape estimation algorithm based upon a level set method [42]. In 2007, Hou examined the construction of imaging functions for several types of scatterer boundary conditions (i.e. scatterer properties) [43] which were used to determine the location of the target and its boundaries using a prior estimation of the number of singular values associated with the target subspace. The number of target associated eigenstates was determined by comparing ratios of singular values to a predetermined threshold. It was observed during numerical experiments that the resolution of the focusing is found to improve when estimated boundary conditions considered for the imaging functions match actual boundary conditions at the scatterer. Carin [44] presented similar observations in presence of a strong scatterer, the waveguide characteristics which are unknown and supposed for the TR imaging of the scattered field can be adjusted until an optimum focusing is reached.

Chapter 3

Modeling of the virtual TR mirror approach

3.1 Introduction

In order to predict the performance of the concurrent detection classification and localization method based on Time Reversal, a numerical model of the virtual TR mirror approach is implemented. The model allows the localization of the seabed targets by transmitting the singular vectors of the TR operator (see Chapter 2) and also provides valuable insights into the method's limitations,. Since the backpropagation does do not involve actual transmissions underwater, the process is referred to as a "virtual Time Reversal mirror". In order to meet the limited power constraints imposed by autonomous operations, the amount of computations involved is minimized by making appropriate simplifications on the modeling. The steps taken to simulate the target insonification, target scattering, and scattered field measurements are described in the first section of this chapter with an emphasis on the underlying theory. The second section explains the implementation of the virtual TR mirror, presents results and summarizes observations made from the simulations.

3.2 Scattered field modeling

An overview of the modules involved in the modeling of the virtual TR mirror approach is shown on Fig. 3-1.

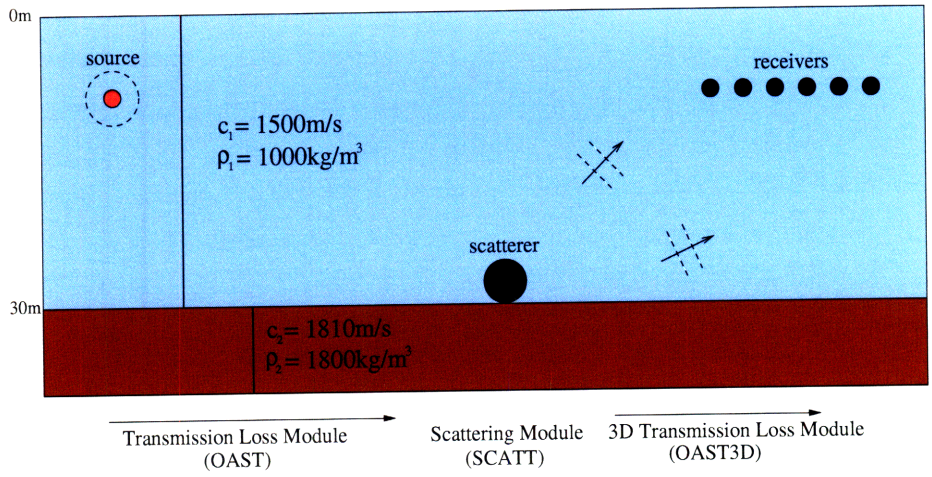

Figure 3-1: Overview of the modeling steps

3.2.1 Target insonification - OAST

The waveguide characteristics considered in this section are chosen to reflect the sea trial during which the virtual TR mirror approach was tested. The sea trial was conducted during the winter of 2008 in a shallow waveguide (30m deep). For modeling purposes, we assume an isospeed water column of 1500m/s. In absence of bottom properties measurements, we make the assumption of an isospeed bottom and use table values corresponding to a sandy bottom [45]. Considering the previous assumptions and the fact that the bathymetry in the area of the sea trial is roughly constant, the propagation environment is conveniently modeled as a Pekeris waveguide.

In a range independent waveguide, the Helmholtz equation satisfied by the total field in each layer takes the following form[1]:

$$[\nabla^2 + k^2(z)]\psi(\mathbf{r}) = f(\mathbf{r}) \tag{3.1}$$

where k is the wavenumber, ψ the field parameter of interest and r is the position vector

A common approach to solving the Helmholtz equation (3.1) is the use of integral transforms: the total field is decomposed into plane waves defined by their individual horizontal wavenumbers. This approach simplifies the treatment of the boundary conditions at each layer interface of the waveguide. The Hankel transform pairs are given by:

$$f(r,z) = \int_0^\infty f(k_r,z)J_0(k_r r)dk_r \tag{3.2}$$

$$f(k_r,z) = \int_0^\infty f(r,z)J_0(k_r r)dr \tag{3.3}$$

The Hankel transform applied to the Helmholtz equation reduces the three dimensional Helmholtz equation 3.1 to the following depth-separated wave equation :

$$\left[\frac{d^2}{dz^2} + (k^2 - k_r^2)\right]\psi(k_r,z) = S_\omega \frac{\delta(z-z_s)}{2\pi} \tag{3.4}$$

where S_ω is the source strength at the frequency ω, k_r is the wavenumber in the radial direction, and z_s is the depth of the source.

The solution of the depth-separated wave equation is obtained using the Direct Global Matrix (DGM) approach. The field within each layer of the waveguide is represented in terms of source contributions and unknown scalar fields amplitudes of up and down going conical waves [46] [47] [5]. The unknown scalar fields which are superposed to the fields resulting from the source contributions are integrated into local sets of equations which are then mapped into a global set of equations solved simultaneously for the amplitude of the

[1] we provide the reader with several of the key equations given in [45]

unknown scalar fields within all the layers. The implementation of this method involves some complexity but this approach is unconditionally stable.

Once the depth-separated wave equation has been solved, the field parameters of interest are determined in the waveguide at any given range and depth by evaluating the inverse Hankel transform (Eq. 3.2) using the Fast Fourier approximation. For practical purposes, the integration domain of Eq. 3.2 is truncated to the largest wavenumber providing significant kernel contribution. The reader can refer to [45] for the detailed derivations.

The waveguide insonification from an omnidirectional source is modeled with OAST, the transmission loss module of the OASES package (Ocean Acoustics and Seismic Exploration Synthesis) developed by H.Schmidt [48]. OASES is a propagation model based on wavenumber integration and the Direct Global Matrix approach. It supports a large variety of environmental models including isovelocity fluids, fluids with speed gradient, isotropic elastic media. The transmission loss module takes as inputs the depth of the source and the characteristics of each homogeneous layer constituting the waveguide (depth of the layer boundaries, fluid density, compressional/shear sound speeds, attenuation coefficients). Since we are concerned with the modeling of a Pekeris waveguide, only three layers are necessary: the upper half space, the water column layer, the sea bottom layer. Solutions are provided in the frequency domain and time domain analysis is obtained by Fourier synthesis. In order to compute the field in the vicinity of a scatterer, OAST accepts as an input the range from the source to the scatterer and the layer where the target is located.

3.2.2 Scattered field - SCATT

The scattering module of OASES called SCATT uses the incident field computed in the vicinity of the scatterer to determine the resulting scattered field using the virtual sources approach. The virtual sources approach consists in replacing the scatterer by a set of sources distributed within its volume. The strength of each source is determined so that

the field produced by the virtual sources when superimposed to the incident field, satisfies the boundary conditions imposed by the type of scatterer. In the case of elastic targets, the dynamic stiffness matrix relates the pressure on the surface of the scatterer to the normal displacement of its surface. We follow several of the step of [3] to describe the computation of the virtual source strengths.

The total pressure $\mathbf{p}$ and total displacement $\mathbf{u}$ on the surface of the scatterer are first expressed as:

$$\mathbf{p} = \mathbf{p}_i + \mathbf{p}_s \qquad \mathbf{u} = \mathbf{u}_i + \mathbf{u}_s \tag{3.5}$$

where $\mathbf{p}_i$ and $\mathbf{u}_i$ refer to the incident field contribution. $\mathbf{p}_s$ and $\mathbf{u}_s$ refer to the scattered field contribution.

Considering a set of N virtual sources of strengths s, the scattered field contribution is expressed as:

$$\mathbf{p}_s = \mathbf{P}\mathbf{s} \qquad \mathbf{u}_s = \mathbf{U}\mathbf{s} \tag{3.6}$$

where $\mathbf{P}$ and $\mathbf{U}$ are $N \times N$ matrices containing the pressure and normal displacement Green functions.
The total pressure is then related to the total displacement through the dynamic stiffness matrix $\mathbf{K}$ as follows:

$$\mathbf{p} = \mathbf{K}\mathbf{u} \tag{3.7}$$

It is important to note that the stiffness matrix of the target is computed independently of the medium that surrounds it and can be used to treat scattering problems for different burial depth and target orientation. The stiffness matrix can be computed with an exact spherical harmonics representation in the case of spherical shells or with a finite element method for objects of arbitrary shapes. Combining Eq. 3.5, 3.6 and 3.7, the source strengths are computed using the following equation:

$$\mathbf{s} = [\mathbf{P} - \mathbf{KU}]^{-1}[\mathbf{Ku}_i - \mathbf{p}_i] \tag{3.8}$$

The scattering module of OASES, SCATT, is used to compute the virtual source strengths associated with various scatterer geometries and properties. In the special case of spherical targets, the command **sphcvs3d** takes the characteristics of the scatterer as an input to compute the virtual source strengths and the scattered field in the surrounding medium can be obtained from the spectral Green functions.

3.2.3 Transmission of the scattered field to the receiving array

Given the distribution of virtual sources and their respective strength, the Green functions from the virtual sources to the surrounding medium are computed with the command OAST3D. Since the virtual sources are distributed in a volume generally much smaller than the region of interest, the scattered field is conveniently derived in a cylindrical coordinate system [49]. Within each layer of the stratified surrounding medium, the scattered field is expressed as the superposition of the field produced by the virtual sources present (if any) and the unknown field required to satisfy the boundary conditions at the layers interfaces. It is governed by the homogeneous wave equation. In a horizontal fluid layer, the resulting displacement potential is expressed with an azimuthal Fourier series as follows:

$$\phi(r,\theta,z) = \sum_{m=0}^{\infty} [\phi_S^m(r,z) + \phi_H^m(r,z)] \left\{ \begin{array}{c} \cos\ m\theta \\ \sin\ m\theta \end{array} \right\} \tag{3.9}$$

where $\phi_S^m(r,z)$ is the contribution from the virtual sources and $\phi_H^m(r,z)$ the contribution that satisfies the layers boundary conditions. Each contribution can be expressed in terms of horizontal wavenumber integrals as follows:

$$\phi_S^m(r,\theta,z) = \frac{\epsilon_m}{4\pi} \int_0^\infty \left[\sum_{j=1}^N s_j \left\{ \begin{array}{c} \cos\ m\theta_j \\ \sin\ m\theta_j \end{array} \right\} \times J_m(k_r r_j) \frac{e^{jk_r|z-z_j|}}{jk_z} \right] k_r J_m(k_r r) dk_r \tag{3.10}$$

$$\phi_H^m(r,\theta,z) = \int_0^\infty [A_m^+(k_r)e^{jk_z z} + A_m^-(k_r)e^{-jk_z z}]k_r J_m(k_r r)dk_r \tag{3.11}$$

where k_r and k_z are respectively the horizontal and vertical wavenumber, s_j is the j^{th} virtual source strength to be determined and A_m^+ and A_m^- are the azimuthal Fourier coefficients of the up and down-going planes waves satisfying the boundary conditions in each layer. The factor ϵ_m equals 1 for $m = 0$ and 2 otherwise.

For the case where both virtual sources and receivers are located in the water column, the Green function becomes:

$$\begin{aligned} G_\omega(\mathbf{r}_i,\mathbf{r}_j) &= s_j \tfrac{e^{jk_1|\mathbf{r}_i-\mathbf{r}_j|}}{4\pi|\mathbf{r}_i-\mathbf{r}_j|} + s_j \textstyle\sum_{m=0}^{\infty} \left\{ \begin{array}{c} \cos\ m\theta_i \cos\ m\theta_j \\ \sin\ m\theta_i \sin\ m\theta_j \end{array} \right\} \\ &\quad \times \tfrac{\epsilon_m}{4\pi} \textstyle\int_0^\infty \left[J_m(k_r r_j) R_{11}(k_r) \tfrac{e^{jk_{z;1}(z_1-z_j-z_i)}}{jk_{z;1}} \right] \\ &\quad \times k_r J_m(k_r r_i) dk_r \end{aligned} \tag{3.12}$$

3.3 Modeling implementation

The commands involved in the modeling described in sections 3.2.1, 3.2.2 and 3.2.3 are executed from a Matlab code. The position of the source and receivers are expressed in a Cartesian coordinate system centered on the elastic target. Using this representation, the computation of distances between the elements of the setup reduces to simple vector calculus operations. This coordinate system also simplifies the grid points representation of the seabed described in the next section. The simulations involve a set of stationary receivers and a set of stationary sources all located at the same depth. The target modeled here is the GOATS sphere and we consider for the clutter a rigid spherical shell of dimensions identical to the GOATS sphere. Each insonification from one of the source location yields a set of complex pressures at the receivers which are stored to construct the interelement matrix. For each of the frequencies of the insonifying signal, the interelement matrix is determined in order to produce the singular values and singular vectors associated with each scatterer over the frequency band of the insonifying signal.

3.4 Virtual Time Reversal Mirror

The previous section of this chapter describes the steps taken to model the waveguide insonification and the scattering from targets present in the waveguide. The complex pressures at the receivers obtained from this numerical model or from actual measurements are used to virtually transmit the time reversed scattered field from the receivers to the seabed and localize the scatterers present.

In the modeling framework introduced above, the seabed is represented as a grid (Fig. 3-2) that extends over the operating area of the AUV. The pressure amplitudes resulting from each backpropagations on the seabed are computed at every point of the grid. The Green functions required to calculate the pressure field on the seabed from the complex pressure at the receivers are precomputed using the **oasp** command for predefined source depths, frequencies and waveguide characteristics. At run time, the real and imaginary part of the Green functions are interpolated at the radial distances of each grid point. Since the waveguide is assumed to be range independent and the receiving array assumed to be horizontal, the same set of Green functions is used to compute the field produced on the seabed by all elements of the array. The resolution of the grid can be adjusted to reduce the time of computation or improve the resolution.

The backpropagation of the singular vectors can also be computed in free field as it will be discussed in the next chapter. The pressure at each grid point of the seabed is then determined by the cross product of the singular vector with the propagation vector M defined by :

$$M = \left(\frac{e^{-jk|\mathbf{r}-\mathbf{r_1}|}}{|\,\mathbf{r}-\mathbf{r_1}\,|}, \frac{e^{-jk|\mathbf{r}-\mathbf{r_2}|}}{|\,\mathbf{r}-\mathbf{r_2}\,|}, \ldots, \frac{e^{-jk|\mathbf{r}-\mathbf{r_n}|}}{|\,\mathbf{r}-\mathbf{r_n}\,|} \right) \tag{3.13}$$

where $\mathbf{r}$ refers to the position vector of the grid point and $\mathbf{r_j}$ refers to the position vector of the j^{th} receiver.

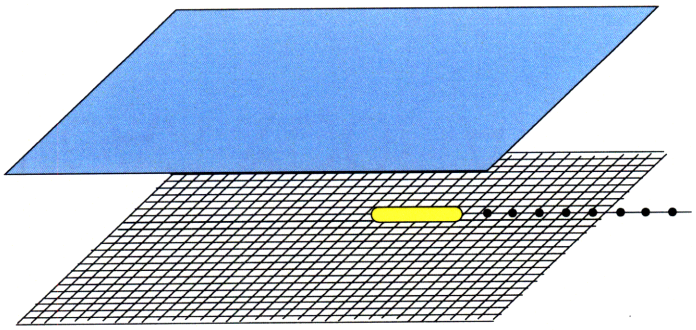

Figure 3-2: Grid representation of the seabed

3.5 Results and observations

The modeling described in sections 3.2 and 3.4 is used to test the ability of our TR based approach to reject clutter and localize seabed scatterers in configurations similar to the set up of the sea trial presented in chapter 4. For the following, we consider a set of stationary sources and a set of stationary receivers located at the same depth in a shallow water waveguide. The targets to be detected and localized are an elastic spherical shell and a rigid spherical shell. Multiple scattering effects between targets are neglected.

3.5.1 Clutter rejection

It was discussed in the second chapter that the response of elastic targets exhibits resonances which are not present in the response of rigid objects. In order to illustrate this point, the TR operator is constructed using the modeling of our approach in presence of an elastic spherical shell and in presence of a rigid spherical shell of identical dimensions. Fig. 3-3 depicts the amplitude of the first singular values for both targets as a function of frequency. The singular value associated with the elastic sphere clearly exhibits a resonance near 900Hz. In contrast the singular value associated with the rigid sphere does not show significant variations over the same frequency band. For elastic targets, the time of arrival of the Lamb-type waves re-radiated in the direction of the receivers varies depending on the array position and orientation. Therefore, the interference of these waves results at the receivers in time signals that differ significantly depending on the configuration source target receivers. As a consequence, the frequencies at which the singular values have maxima

can not directly be used to classify the target; instead the variability of a singular value with respect to frequency can be used to classify a target as rigid or elastic.

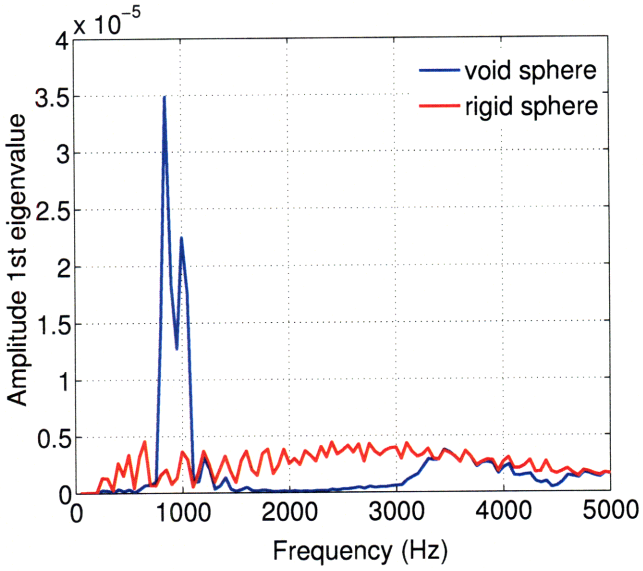

Figure 3-3: Amplitude of the first singular value as a function of frequency for a void elastic sphere and a rigid sphere

It is also important to observe from Fig. 3-3 that the dominant singular value is not necessarily associated with the same scatterer throughout the whole frequency band. The backpropagation of the first singular vector therefore results in a field that focuses on the dominant scatterer at the frequency of interest.

3.5.2 Selective focusing

We investigate in this section the ability of the virtual TR mirror approach to localize targets on the seabed. The scattered field computed at the receivers in presence of an elastic target and a rigid target is used to construct the TR operator. The backpropagation of the eigenvectors associated with each targets is achieved using the virtual Time Reversal mirror approach described in section 3.4. The receiving array considered here is composed of 20 elements spaced every 0.75m for a total length of 14.25m. In presence of well resolved scatterers (i.e scatterers separated by a distance larger than the resolution cell), the singular vectors of the TR operator provide the phase and amplitude information to focus selectively on each scatterer present. Fig. 3.4(a) and 3.4(b) show respectively the field backpropagated on the seabed for the transmission of the singular vector associated with the elastic target located at (0,0) and the singular vector associated with the rigid target located at (-20,0). We observe that the transmission of each singular vector shows a maximum at the location of each corresponding scatterer. The size of the retrofocus is related to the resolution of the array. For the smaller array extent considered during the sea trial, we expect a decrease in resolution.

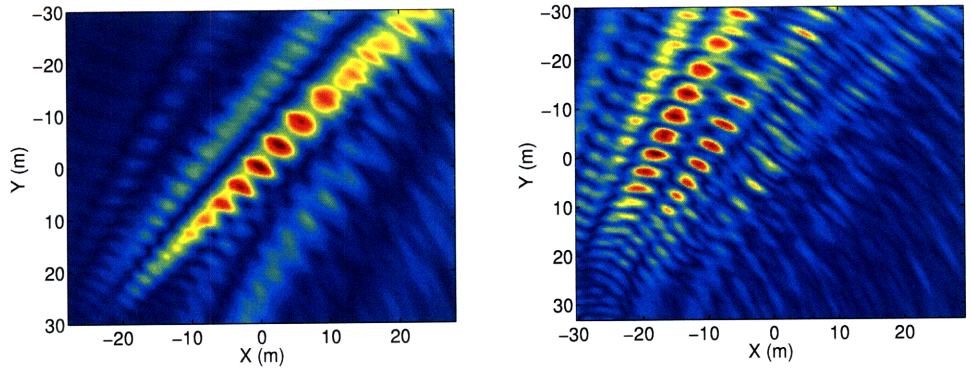

(a) Focusing on the elastic target

(b) Focusing on the rigid target

Figure 3-4: Backpropagation of singular vectors associated with an elastic sphere located at (0,0) and a rigid sphere located at (-20,0) compensated for spherical spreading

Chapter 4

Experimental validation

4.1 Introduction

The virtual TR mirror approach is tested with a set of experimental data collected near the island of Palmaria (Italy) on the 25th of January 2008. The first section of this chapter provides a description of the setup of the CCLNet08 trial. The steps taken to process the data collected are explained in the second section. The last part of the chapter concludes with the results of the processing.

4.2 Experimental configuration

4.2.1 Description of the sea trial

One of several objectives of the CCLNet08 sea trial described in this chapter was to collect scattered field measurements in presence of seabed objects. The waveguide was insonified with an omnidirectional source towed behind a research vessel (Leonardo) and the acoustic field scattered by the seabed objects was sampled with an array of hydrophones towed behind an Autonomous Underwater Vehicle (Ocean EXplorer or OEX version C) (Fig. 4-1).

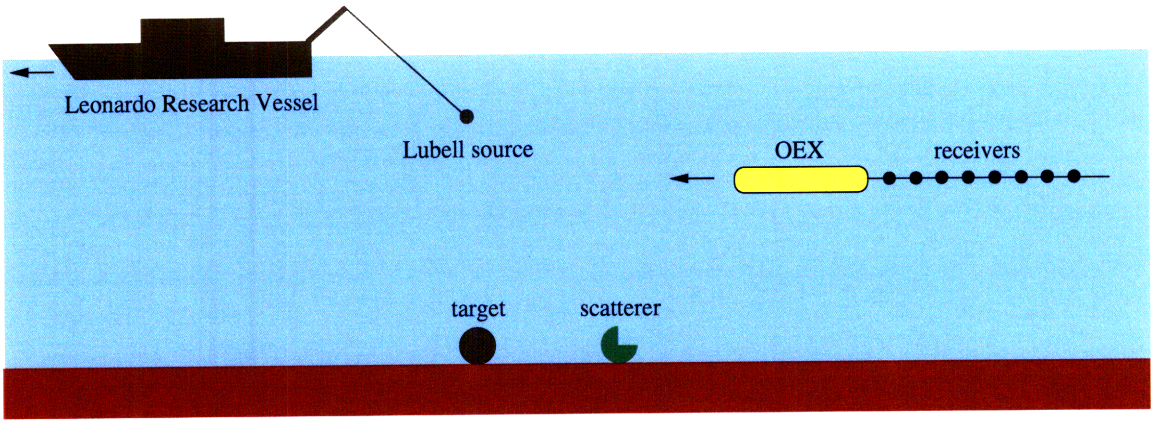

Figure 4-1: Side view of experimental setup

The choice of a bistatic configuration is best suited to sample efficiently the anisotropic scattered field from the seabed targets. Fig. 4-2 shows the path of the Leonardo and of the OEX during the run as well as the positions of the scatterers in local grid coordinates. Both vehicles started their mission at the north east of the scatterers then moved west, south and east. Over the course of the mission, the scatterers were successively located at endfire and broadside relative to the receiving array.

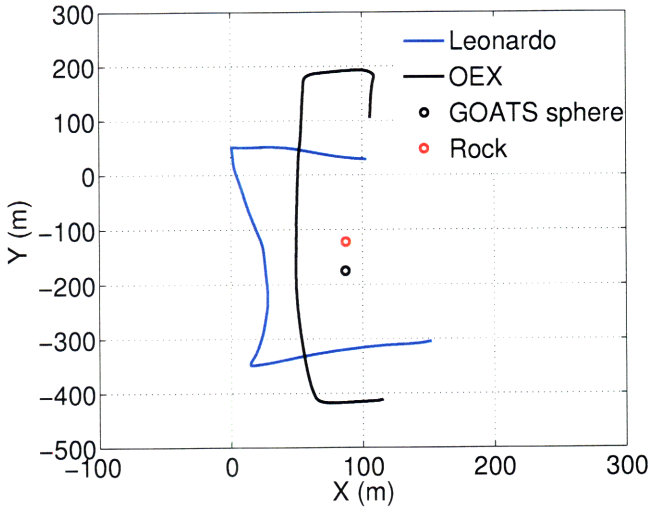

Figure 4-2: Location of the OEX and Leonardo during the run

The targets to be detected and localized are an elastic sphere and a rock. Prior to the experiment, the targets were lowered on the seabed and their GPS location logged. The elastic target referred to as the GOATS sphere is hollow, made of steel (density 7700

kg/m^3, compressional wave speed 5950m/s shear wave speed 3240 m/s). The shell outer radius and wall thickness are respectively 0.53m and 0.03m. The scattering strength of the GOATS sphere is known from past numerical modeling investigations and experimental measurements (Fig. 4-3). The rock which played the role of clutter is of comparable size and its scattering strength is also known. The two targets were separated by a distance of 50m.

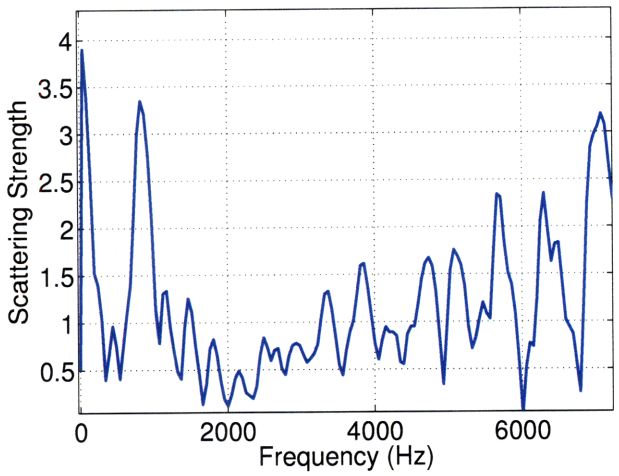

Figure 4-3: Experimental scattering strength of the GOATS sphere

4.2.2 Waveguide insonification

The waveguide is insonified with a Lubell source (Ref. LL1424HP) which transmits a 1-ms Ricker pulse[1] centered at 2kHz with a ping rate of 4Hz. Fig. 4.4(a) and Fig. 4.4(b) show respectively the Ricker pulse applied to the Lubell source in the time domain and in the frequency domain. The short duration of the pulse provides the spatial resolution suitable for localization purposes and the low frequency band allows for a higher coverage rate.

Before the beginning of the run, the source is lowered at a depth of 10m and calibrated by measuring its sound pressure level 13m away from its center for applied driving voltage of frequency varying from 0.1kHz to 5kHz. Fig. 4-5 and Fig. 4-6 show respectively the

[1]The Ricker pulse is defined as the second derivative of a Gaussian

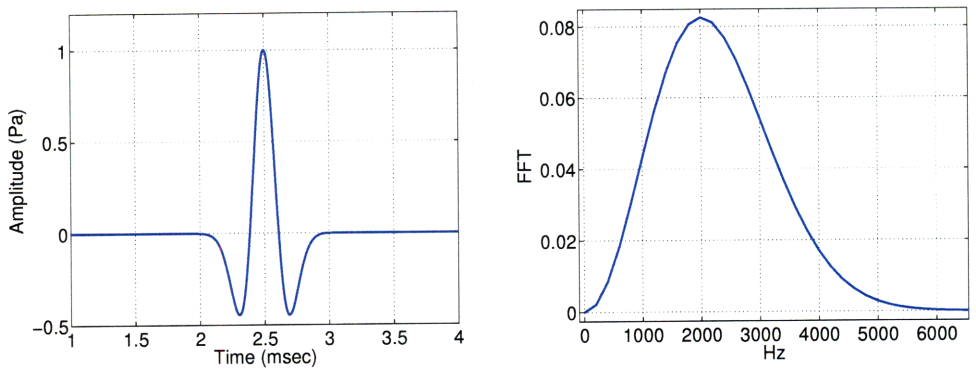

(a) Time domain (b) Fourier transform

Figure 4-4: Ricker pulse applied to the Lubell source

calibration setup and the Transmitting Voltage Response measurements.

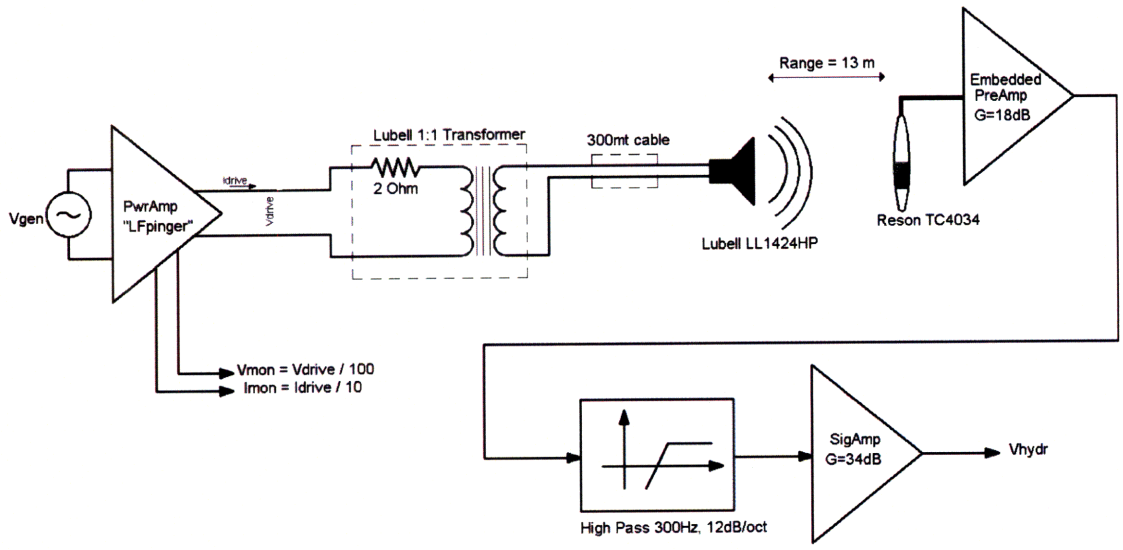

Figure 4-5: Calibration setup of the Lubell source

4.2.3 Data acquisition

The SLITA (Slim LIne Towed Array) receiving array consists of 48 hydrophones distributed in 2 octave spacings: 0.211m and 0.422m. The processing described in this chapter is concerned with the measurements from the 32 hydrophones spaced every 0.211m. The hydrophones (Benthos AQ-4) have a sensitivity of 201dB ref 1 Volt per μPa and are de-

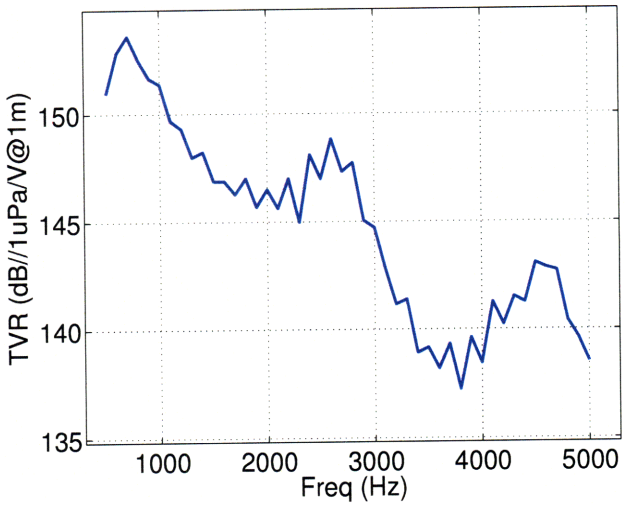

Figure 4-6: Transmitting voltage response of the Lubell source measured during calibration

signed to compensate for acceleration noise [50]. During the mission, the acoustic field is sampled with an A/D board (PCI-24DSI32) at an acquisition rate of 51kHz and with a 24 bits resolution. Every 4 seconds, the data acquisition system produces a binary file that contains the time series of each of the 32 channels. Continuous measurements were conducted during the mission of the OEX which started at 11.34am and finished at 1.14pm local time on the 25th of January 2008. Our processing is limited to the part of the run during which the distance between the source the target and the receivers ensures sufficient signal to noise ratios.

4.2.4 Environmental data

As explained in section 3.2.1, the bathymetry data available in the region of the sea trial indicates that the depth of the waveguide is approximately constant and equal to 30m. The sound speed profile in the winter time in a very shallow waveguide is assumed to be constant over the whole water column and was estimated to be 1500m/s. The sound speed of the sandy bottom was not measured and the value of the compressional sound speed was assumed to be 1800m/s.

4.3 Processing

4.3.1 Estimation of the source and receivers locations

In order to compute the time of arrival of the target and rock reflected echoes, the location of the receivers and of the source during the mission must be estimated. This section describes the steps taken to estimate precisely their location during the run.

The location of the hydrophones is determined from the logs of the OEX and the specifications of the SLITA array. Before the dive, the Global Positioning System (GPS) of the OEX provides its location. During the mission, the navigation system of the OEX uses its initial GPS fix as a reference to estimate its future positions from dead-reckoning and DVL measurements. The GPS fix taken after the vehicle surfaces at the end of the mission, is used to correct for navigation errors that occured during the run. In the local grid coordinate system, the cumulated navigation error was found to be of 2.74m in the x direction and 34m in the y direction. Since the SLITA files processed were produced toward the end of the run, the corresponding vehicle locations are assumed to be affected by the same navigation error and the same correction is applied.

The location of the receivers relative to the AUV are estimated by replaying the logs of the OEX in a simulation environment [51] and running in parallel a dynamic array model. The model takes as inputs the speed of the OEX logged during its missions and the characteristics of each section of the array (number of subsections, weight in water, diameter, tangential and normal drag coefficient, modulus of elasticity). The SLITA array is composed of 3 main sections: the extension module, the acoustic module and the tail and the number of subsections is chosen to provide a fine element spacing in the extension and the acoustic module. Given the previous (or initial) shape estimate and the current tow point velocities, the model determines the new array shape by applying the Newton-Raphson iteration to solve the set of nonlinear algebraic equations found in [52]. During the run, the depth of the hydrophones is assumed to be equal to the depth of the vehicle provided by its depth sensor.

The location of the source towed behind the research vessel is determined during the run from the GPS measurements of the ship knowing the position of the towing point relative to the center point of the ship. The length of the ship is 28.6m and the distance between the GPS positioned on the mast and the towing point was estimated to be 17m. Due to the short length of the towing cable, it is assumed to remain straight and to point in the direction of motion of the ship. Before the beginning of the mission, the source is lowered at a depth of 10m while the ship has zero forward speed and during the mission a sensor mounted on the source records its depth (Fig. 4-7).

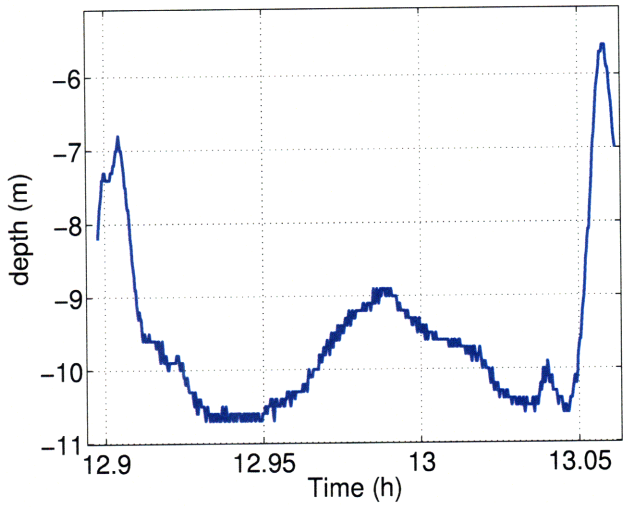

Figure 4-7: Depth of the Lubell source during the run

Finally, the timestamps of the logs of the Leonardo take as a reference the GPS absolute time while the timestamps of the logs of the OEX and of the SLITA files take as a reference the clock of its payload. At the end of the run, the payload clock was found to be 28 secs out of synchronization with the GPS time. This additional correction was applied to the timestamp of each AUV location and each SLITA file timestamp.

4.3.2 Validation of the source and receivers location estimations

The processing of multipath echoes is irrelevant to our analysis since they do not interact with the target or the rock. However, their time of arrival can be used to verify that the source and receiver locations are correctly estimated after the navigation and synchronization errors have been accounted for. Since the wavelength of the insonifying signals are much shorter than the characteristics lengths of the waveguide, the time of arrivals of each multipath echo is predicted from ray theory and using the source and receivers locations estimate during the run. The experimental time of arrival are determined from the signals measured at each hydrophone. The binary SLITA files produced by the data acquisition system of the OEX during the mission are converted to voltage time series of each channel using a Matlab script provided by M. Mazzi. The following analysis is concerned with the processing of the measured signals in the frequency band of the Ricker pulse (0-6kHz) used for insonification. Prior to the processing, the signals are low pass filtered with Butterworth filter of order 10 and a cut-off frequency of 12kHz.

The strongest arrivals present in the time signals measured at the hydrophones are associated with the direct path between the source and the receivers. Each time series is matched filtered with the first direct arrival to determine precisely the following direct arrival times. Once the later have been detected, the time series are divided into time windows of 250 milliseconds and staked to reveal the common features of the pings and facilitate the post processing.

Fig. 4-8 shows a small set of pings stacked together. We can see from the figure that the direct arrival is followed by the surface reflected arrival which is an inversed and slightly attenuated replica of the direct arrival (due to the phase inversion of the signal at the pressure release surface). The following multipath echoes are associated with paths depicted in Fig. 4-9: bottom reflected, bottom-surface reflected, surface-bottom reflected etc.

The experimental arrival times of the multipath echoes are compared to predicted ar-

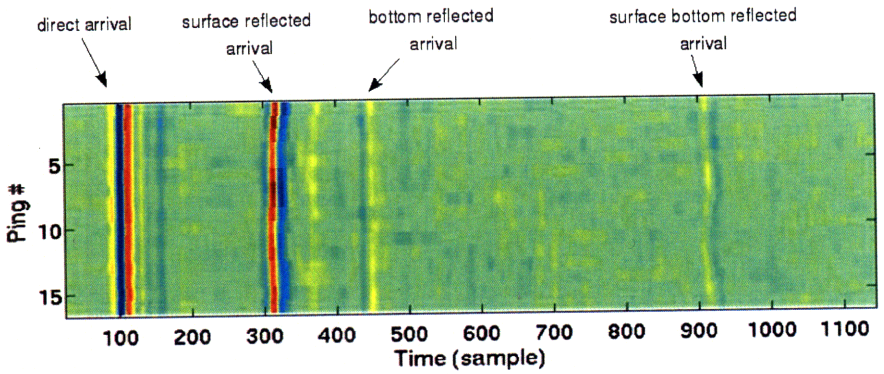

Figure 4-8: Stack of pings

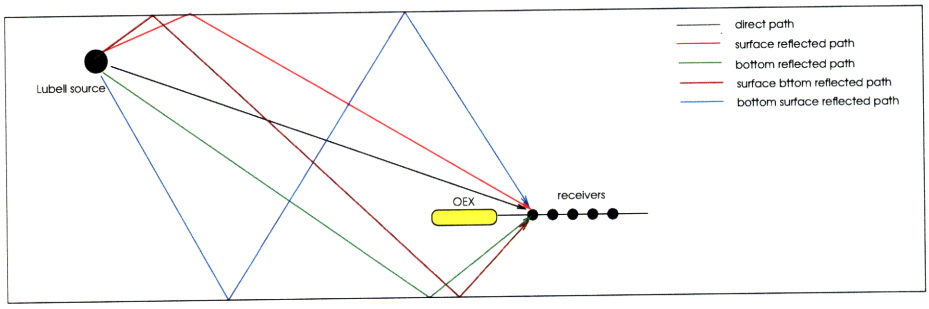

Figure 4-9: Multipath between the source and the receivers

rival times inferred from geometrical considerations for the first receiver. Fig. 4-10 shows the predicted time of arrival of the direct arrival followed by the multipath arrivals for the pings of the run. Fig. 4-11 shows for the same set of pings, the amplitude of the experimental signals stacked as in Fig.4-8. The good match between predicted and experimental arrival times validates the set of corrections applied in section 4.3.1 and our assumptions on the waveguide characteristics. Since the location of the source and receivers are correctly estimated, the predicted arrival time of the target and rock reflected echo (Fig. 4-10) are also assumed to be correct.

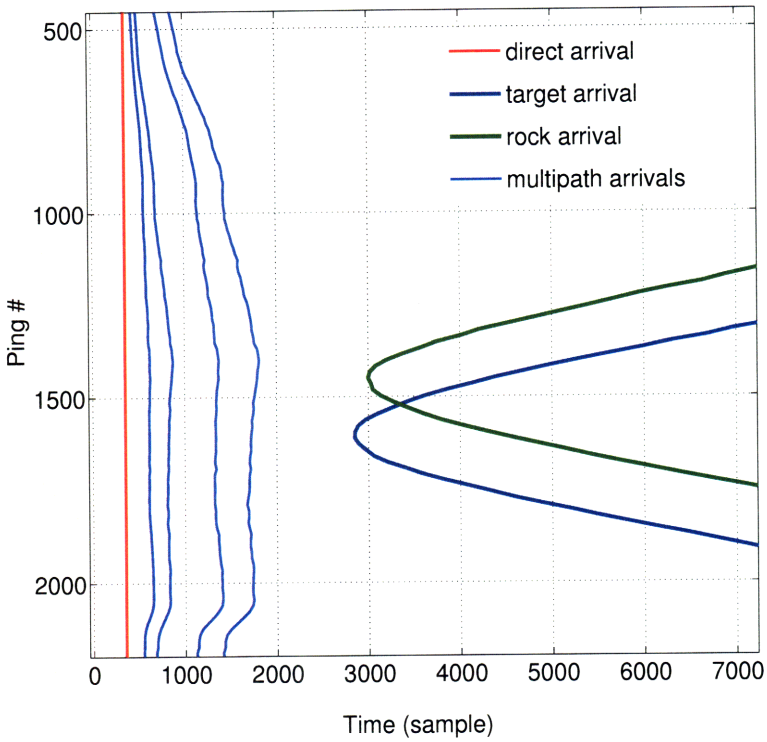

Figure 4-10: Predicted time of arrivals of the multipath echoes

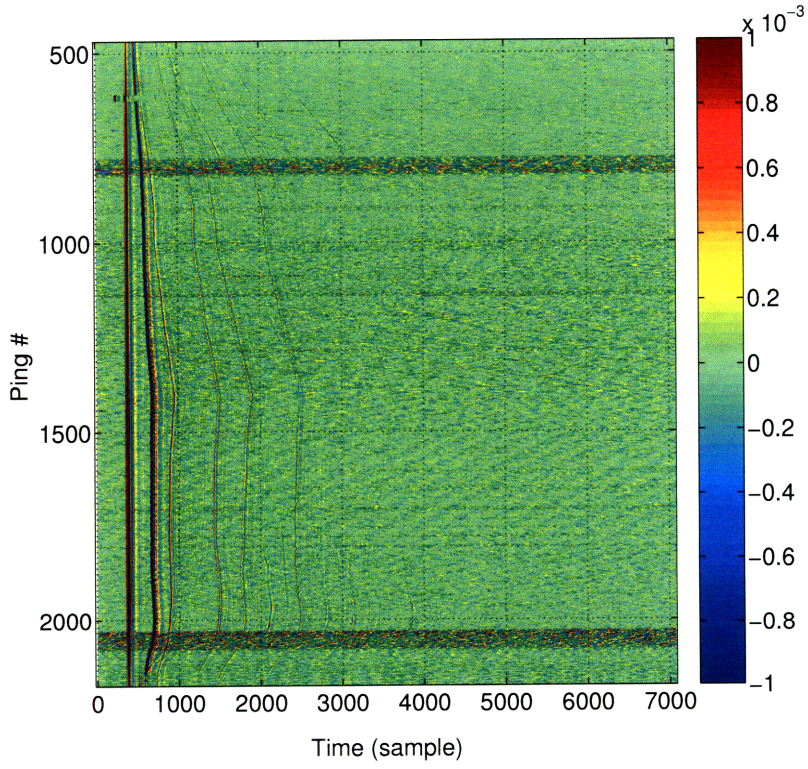

Figure 4-11: Experimental time of arrivals of the multipath echoes

4.3.3 Construction of the TR operator

The construction of the TR operator is based upon the covariance matrix approach introduced in Section 2.1.5. Given the vectors of complex pressures $P_n(\omega)$ measured at the receivers for each of the N source positions, the TR operator is expressed as follows:

$$TRO(\omega) = \sum_{n=1}^{N} P_n(\omega)^t P_n(\omega)^* \tag{4.1}$$

In order to recreate a stationary receiving array from the moving receivers, the largest number of receivers that can be considered is 16. The construction of the TR operator therefore involves 16 successive insonifications that occur over a time period of 4 seconds (which in calm water can be assumed to be smaller than the coherence time of the channel). In practice, the requirement of overlapping receivers at the emission time of the source is not strictly satisfied, but the assumption of a range independent environment allows to report small discrepancy from overlapping positions as a delay in the time of emission. Insonifying the waveguide from an omnidirectional source as in the sea trial results in significant transmission losses caused by the geometrical spreading and the attenuation of the portion of the transmitted field incident on the seabed at supercritical angles. The presence of sources of noise during the mission also reduces the signal to noise ratios at the receivers. It was reported that the cavitation at the propeller of the Leonardo introduces a strong permanent noise in the frequency band of the insonifying signal [50]. The self noise of the array and the noise introduced by the propeller of the AUV are both assumed to be dominated by the noise caused by the Leonardo in the frequency band of interest. As a result, the weak echoes from both targets can not be detected visually when stacking pings of the run together. Instead, the arrival times of the targets is determined from the analysis of the singular values of the TR operator constructed for a sliding time window. In order to limit the impact of background noise, the duration of the sliding time window over which the TR is computed needs to be reduced to 5ms with an overlap of 80%. This window duration is sufficiently long to include both the specular echo of the target and its elastic response if present [1] while the overlap of 80% allows to determine more precisely the arrival time of each echo.

4.4 Results

4.4.1 Detection of the target and rock echoes

As explained in the second chapter, each singular value and corresponding eigenvector is associated with an invariant of the TR process. With respect to the experimental setup, we expect that the propeller of the Leonardo which constitutes a strong permanent source of noise will introduce at least one singular value which may dominate the singular values associated with the scatterers to be detected. Since the measured signals were observed to have very low amplitude above 3kHz, the following figures only show the frequencty band [0-3kHz].

Target echo

Fig. 4-12 and 4-13 show the amplitude of the four largest singular values in a time window that contains the echo from the target. For the set of pings used to construct the TR operator, the echo from the target is predicted to occur at sample 2900. This predicted time of arrival coincides with the time at which the amplitude of the third singular value exceeds that of the background noise. We suspect that the first singular value is associated with the Leonardo while the fourth and remaining singular values are associated with the background noise.

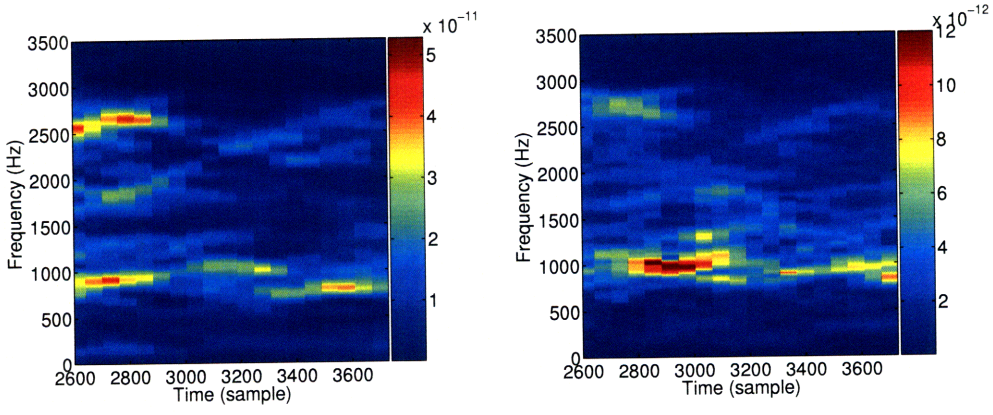

(a) 1st singular value

(b) 2nd singular value

Figure 4-12: Elastic target echo - First and second singular value

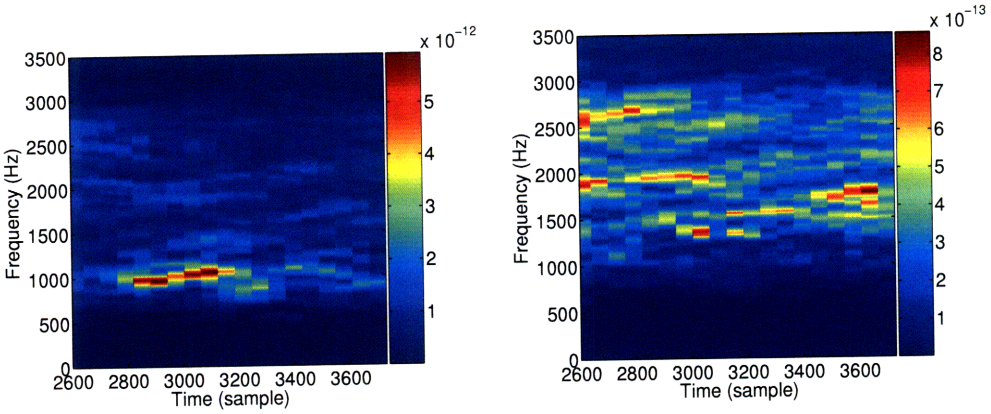

(a) 3rd singular value

(b) 4th singular value

Figure 4-13: Elastic target echo - Third and fourth singular value

Rock echo

Fig. 4-14 and 4-15 show the amplitude of the four largest singular values in a time window that contains the echo from the rock. For the set of pings used to construct the TR operator, the echo from the rock is predicted to occur at sample 3100. This predicted time of arrival coincides with the time at which the amplitude of the third singular value exceeds that of the background noise 4.15(a). It is unclear from the observation of the first and second singular values if they are associated with the echo from the rock or with the propeller of the Leonardo. The remaining singular values are associated with the background noise.

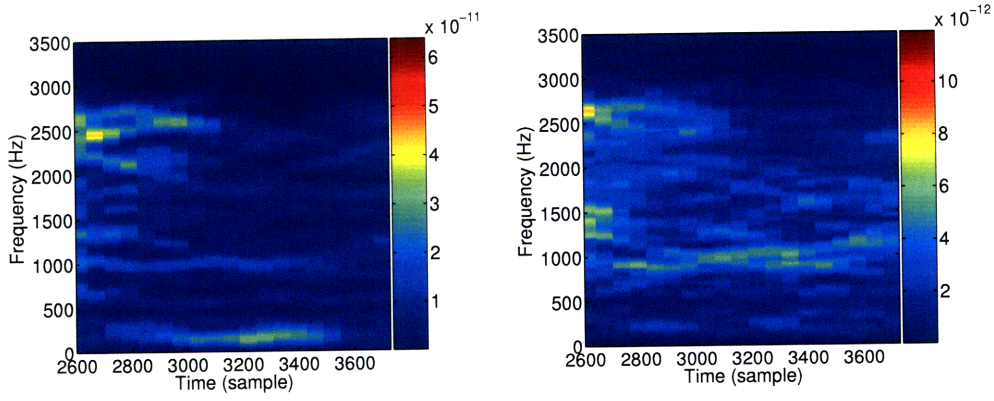

(a) 1st singular value

(b) 2nd singular value

Figure 4-14: Rock echo - First and second singular value

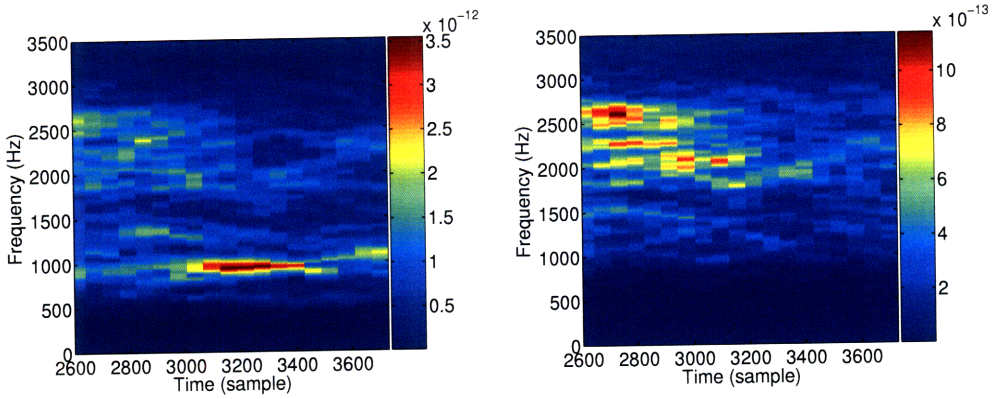

(a) 3rd singular value

(b) 4th singular value

Figure 4-15: Rock echo - Third and fourth singular value

4.4.2 Target localization

In order to determine to which scatterer corresponds each of the singular value depicted in section 4.4.1, the virtual TR mirror approach is used to backpropagate the corresponding singular vector. It was explained in section 4.3.3 that the presence of background noise can be limited by reducing the duration of the time window used to construct the TR operator. This comes at the cost of removing the multipath between the source and the receivers. As a consequence, the resolution during the backpropagation process is reduced and consequently the size of the retrofocus increased. The singular vectors obtained from the decomposition of the TR operator computed for a short time window provides the amplitude and phase to apply to each transducer of the array to focus in free space at a given frequency (neglecting the target bottom reflected path). The resolution cell of the array is defined in free field as follows [29]:

$$R = \frac{\lambda_0 F}{D} \tag{4.2}$$

where λ_0 is the wavelength of the signal transmitted by the TRM, F is to the distance between the target and the array and D is the length of the stationary section of the array (equal 3.165m). For the frequency band of interest, λ_0 varies from 0.25m at 6kHz to 1.5m at 1kHz. At the time when the signals used to construct the TR operator in section 4.4.1 are recorded, the distance F between the target and receivers of the array is approximately

45m and corresponds to a resolution cell of R = 21m at 1kHz and 3.5m at 6kHz.

Elastic target echo

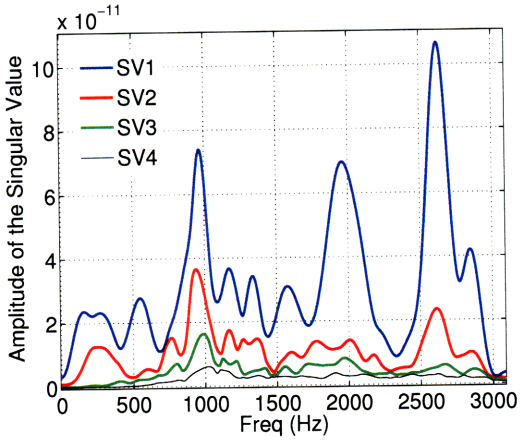

Figure 4-16: Singular Values associated with the echo from the elastic target

The decomposition of the TR operator at the time of arrival of the elastic target echo yields the singular value distribution depicted in Fig 4-16.

Fig 4.17(a) shows the location of the propeller of the Leonardo and the receivers at the time when the TR operators of Fig. 4-12 and Fig. 4-13 are constructed. Fig. 4.17(b) and 4-18 depict a top view of the backpropagated field on the seabed associated with the first three singular vectors. The backpropagated field is compensated for spherical spreading and is depicted for an array pointing in the $-x$ direction and located at the origin (matching the orientation of the array of the experimental setup). The field associated with the transmission of the first singular vector points in the direction of the Leonardo which is consistent with the assumption that the dominant singular value is associated with the noise produced by its propeller. It is unclear if the backpropagated field associated with the second singular vectors points in the direction of the target or in the direction of the propeller of the Leonardo. The backpropagated field associated with the third singular vector does point in the direction of the elastic target which is also consistent with the fact that the time at which the singular value emerges coincides with the predicted time of arrival.

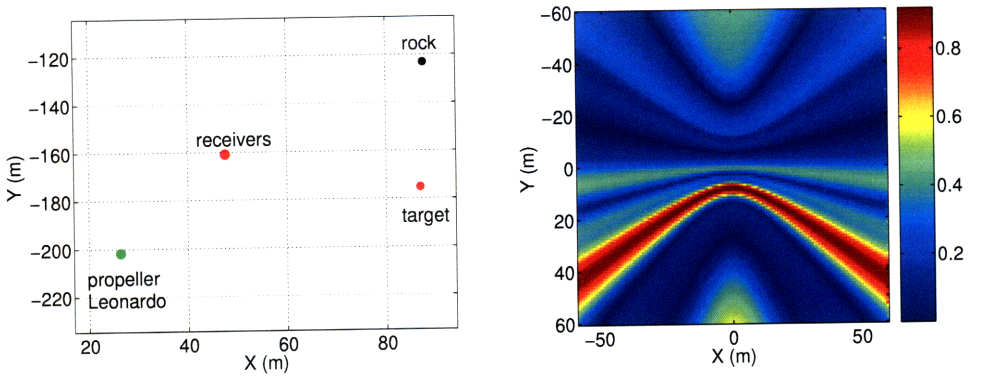

(a) Configuration A

(b) backpropagation of the 1st eigenvector

Figure 4-17: Free field backpropagation of the first singular vector

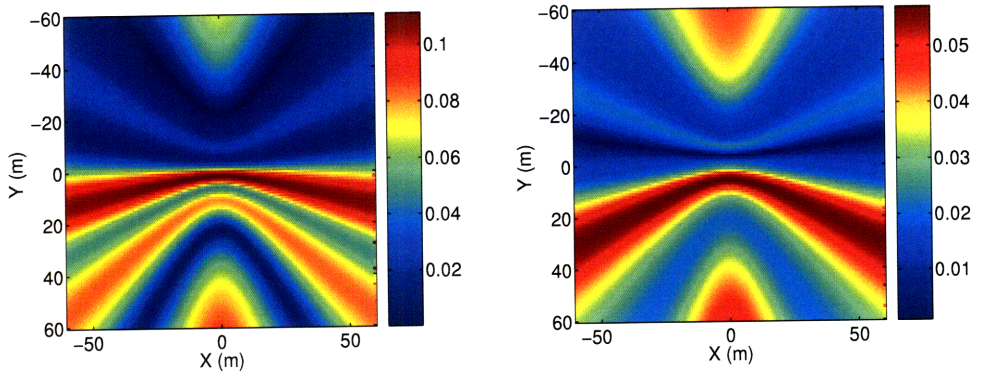

(a) backpropagation of the 2nd eigenvector

(b) backpropagation of the 3rd eigenvector

Figure 4-18: Free field backpropagation of the second and third singular vector

Rock echo

The decomposition of the TR operator at the time of arrival of the elastic target echo yields the singular value distribution depicted in Fig 4-19.

Fig 4.20(a) shows the location of the propeller of the Leonardo and receivers corresponding to the pings from which the TR operators depicted in Fig. 4-14 and Fig. 4-15 are constructed. We observe from Fig. 4.15(a) that the third singular value which is assumed to be associated with the rock, emerges from the background noise at a frequency of 1kHz. The resolution provided by the configuration at this frequency does not allow to separate

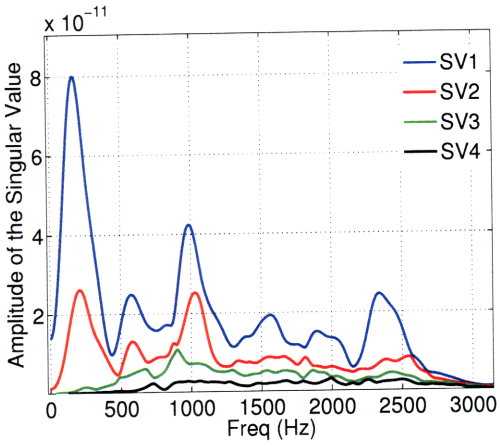

Figure 4-19: Singular Values associated with the echo from the rock

the contribution of the propeller from that of the rock. The backpropagated field corresponding to the first (Fig. 4.20(b)) and third singular vectors (Fig. 4.21(b)) are pointing in the direction of the rock. However the backpropagated field associated with the second singular vector (Fig. 4.21(a)) points in a direction that can not clearly be associated to the rock or the Leonardo.

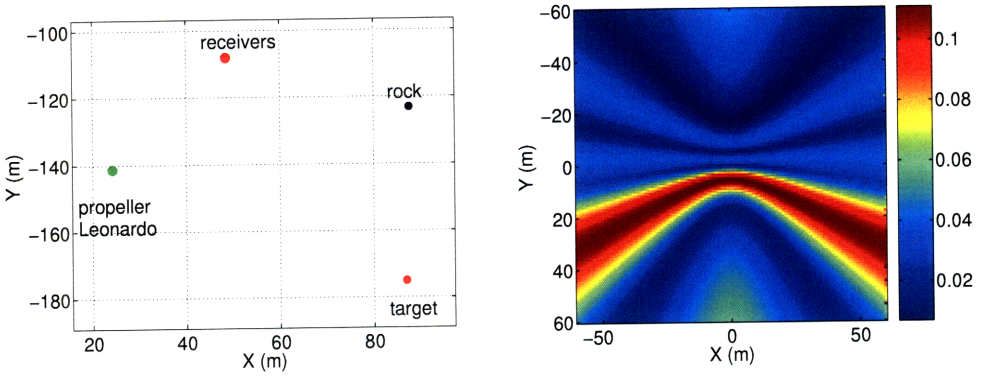

(a) Configuration B

(b) backpropagation of the 1st eigenvector

Figure 4-20: Free field backpropagation of the first singular vector

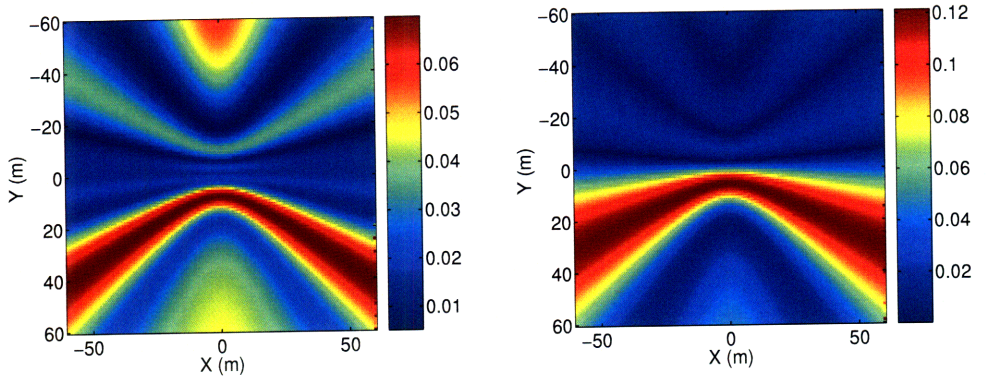

(a) backpropagation of the 2nd eigenvector (b) backpropagation of the 3rd eigenvector

Figure 4-21: Free field backpropagation of the second and third singular vector

It was demonstrated in [31] that the field scattered by an elastic spherical target can be represented in terms of monopole and multipole contributions. In order to be able to resolve the singular values associated with the multipole contributions, the extent of the receiving array needs to be sufficient to capture the angular variations of the corresponding projected harmonics. The configurations source target receivers depicted in Fig. 4.17(a) and Fig. 4.20(a) allow to resolve the isotropic component of the scattered field from both target but do not allow to detect the anistropic field associated with the elastic target scattering. Therefore, the rock and the elastic target appear identical in terms of their singular values and can not be classified. The localization process requires the combination of bearing estimates obtained from the transmission of singular vectors associated with successive sensing points-of-view. The benefit of a bistatic configuration becomes appearent here as it allows for adaptative resolution adjustements needed to classify the targets previously localized.

Chapter 5

Conclusion

5.1 Summary

A virtual TR mirror approach for the detection, localization and classification of seabed objects has been modeled and tested with experimental data. A numerical code was implemented to simulate the broadband insonification (0-6kHz) of elastic and rigid targets from a set of source locations and to determine the resulting pressure fields at a stationary receiving array. The TR operator was constructed using the covariance matrix approach, and it was shown that the analysis of the singular values allows the detection of elastic scatterers by observing the presence of resonance frequencies. The virtual TR mirror approach was modeled and used to localize seabed objects by simulating the backpropagation of their corresponding singular vectors.

The second part of this work involved the processing of scattered field measurements collected at sea in the presence of seabed targets. The location of the source and receivers during the sea trial once determined accurately was used to predict the time of arrival of the echoes from the targets. A permanent source of noise was present during the sea trial measurements. In order to limit its effect, the TR operator was constructed over short overlapping time windows. The analysis of its singular values allowed the determination of the target echoes arrival time which were found to be in good agreement with the predictions based upon geometric considerations. Reducing the duration of the time window when

constructing the TR operator came at the cost of removing contributions from the waveguide boundaries and resulted in a degraded resolution during the backpropagation of the singular vectors. Due to the limited extent of the stationary section of the array, the backpropagation of the singular vectors only allowed an estimate of the bearing to the targets but fails at providing an estimate of their range. Localizing the scatterers with the same array aperture would therefore require a sufficient signal to noise ratio to combine several bearing estimations.

5.2 Future work

One major challenge associated with the virtual TR mirror approach consists in matching each singular value with the corresponding scatterer. It was observed that the presence of permanent sources of noise results in irrelevant eigenstates that need to be identified as such. The classification of targets based upon the singular value analysis also requires to take into account the changes of effective reflectivity associated with each target as the mobile sensing platforms operates. The observation of the singular values with respect to time will have to be investigated further as it may provide ways of tracking these changes and sort the singular values in a systematic manner.

Recreating a stationary array from a set of moving receivers reduces its exploitable aperture which affects the localization process. In that regard, the use of a bi-static configuration provides the flexibility needed for adaptative resolution adjustments and facilitates the classification and localization of seabed targets. However, translating a distribution of singular values into target structural characteristics remains a complex problem that requires to account for varying sensing point-of-views and unknown possible scattered fields. For the virtual TR mirror approach to be exploitable by autonomous platforms, the processing of the singular values will need to be addressed in a systematic manner.

The computational efforts involved in the transmission of the singular vectors have been minimized by considering a range independent waveguide and limiting our analysis to seabed objects. One can anticipate, however, that the backpropagated field on the seabed associated with mid-depth scatterers would yield erroneous location estimations. Extending the domain over which the field is backpropagated would require an adaptive resolution technique in order to limit the amount of computation while allowing the localization of scatterers or sources at different depths.

Appendix A

Matlab User Guide

A.1 Experimental setup - Estimation of echoes arrival time

The following code is used to read the logs produced by the OEX and by the Leonardo and plot their location during the sea trial described in Chapter 4 (see Fig. 4-2). The location of the source and receivers (respectively towed behind the Leonardo and the OEX) are estimated using the ship characteristics and the specifications of the SLITA array. All the locations provided in the logs as latitude and longitude were converted to local grid coordinates to facilitate the computation of distances between the elements of the setup. Using the location of the sources and the first receiver, the code generates the estimated time of arrival of multipath and target reflected echoes (see Fig. 4-10). Several corrections are introduced to compensate for the lack of synchronization between the clock of the payload on the OEX and the GPS time (line 79) and to account for the navigation errors which were evaluated during the post processing (line 302).

```
0001 %--------------------------------------------------------------------------
0002 %                        CCLNet08 EXPERIMENTAL SETUP
0003 %--------------------------------------------------------------------------
0004
0005 % ========================================================================
0006 % LOADING OF LEONARDO AND SOURCE LOGS FOR 01/25/08
0007
0008
0009 % defines origin of local grid coordinate system
0010
0011 LatOrigin = 44.016;
0012 LongOrigin = 9.82;
0013
0014 geo_datum=[LatOrigin LongOrigin];
0015 zone=floor((geo_datum(2)+180)/6)+1;
0016 prime_meridian=zone*6-183;
0017 utm_datum = geo2utm(geo_datum,prime_meridian);
0018
0019 % loads logs of Leonardo
0020
0021 log_leo = load('log_leo.mat');
0022 lat  = log_leo.lat;
0023 long = log_leo.long;
0024
0025 utc_time    = log_leo.utc_time;
0026 local_time  = log_leo.normal_time;
0027
0028 % converts local time of timestamp into milliseconds since midnight
0029
0030 time_ms(:,1) = ((str2num(local_time(:,13:14))+5)*60*60*1000)+ ...
0031 (str2num(local_time(:,16:17))*60*1000)+ (str2num(local_time(:,19:20)))*1000;
0032
0033 % ========================================================================
0034 % LOCATION AND HEADING OF LEONARDO BETWEEN 12:53:36 and 13:03:36 (01/25/08)
0035
0036 % loads heading of Leonardo
0037
0038 A = load('head_leo.mat');
0039
0040 % Note 2441 -> 125336 and  2931 -> 130336
0041
0042 % extract timestamps and location
0043
0044 leo_time_ms             = time_ms(2441:2931,1);
0045 leo_pos_latlong         = [lat(2441:2931,1) long(2441:2931,1)];
0046 leo_head                = A.head(2441:2931,1);
0047
0048 % converts location from lat/long to localgrid
0049
0050 for k1 =1:length(leo_pos_latlong)
0051     pos_leo(k1,:) = geo2utm(leo_pos_latlong(k1,:),prime_meridian)-utm_datum;
0052 end
0053
0054 xy_leo = [pos_leo(:,2) pos_leo(:,1)];
0055
0056 % ========================================================================
0057 % LOCATION, HEADING AND DEPTH OF OEX BETWEEN 12:53:36 and 13:03:36 (01/25/08)
0058
0059 start_run = '125336';
0060 end_run   = '130336';
0061
0062 % starting and ending time of the run converted in milliseconds
0063
0064 start_run_ms = (str2num(start_run(1:2))*60*60*1000) + ...
0065     (str2num(start_run(3:4))*60*1000)+(str2num(start_run(5:6))*1000);
0066 end_run_ms   = (str2num(end_run(1:2))*60*60*1000) + ...
0067     (str2num(end_run(3:4))*60*1000)+((str2num(end_run(5:6)))*1000);
0068
```

```
0069 % AuvPosition_data.m -> OEX location and corresponding milliseconds timestamps
0070
0071 AuvPos = AuvPosition_data;
0072
0073 % delay in sec between OEX and GPS clock
0074
0075 clock_dif = 28;   % time difference between AUV clock and Leonardo (GPS) clock
0076
0077 % corresponding correction in ms
0078
0079 delay = -clock_dif*1000;
0080
0081 % correct AUV clock time to account for delay with GPS time of Leonardo
0082
0083 AuvPosTime = AuvPos.TimeStamp.time_t + delay;
0084
0085 temp1 = abs(AuvPosTime - start_run_ms);
0086 [val ind1] = min(temp1);
0087
0088 temp2 = abs(AuvPosTime - end_run_ms);
0089 [val ind2] = min(temp2);
0090
0091 % extract OEX timestamps - converts lat/long to local grid coordinates
0092
0093 oex_time_ms = AuvPosTime(ind1:ind2,1);
0094 oex_pos_latlong = [AuvPos.AuvPosition.latm.min(ind1:ind2,1) ...
0095                    AuvPos.AuvPosition.longm.min(ind1:ind2,1)]/60;
0096
0097 for k1 = 1:length(oex_pos_latlong)
0098     pos_oex(k1,:) = geo2utm(oex_pos_latlong(k1,:),prime_meridian)-utm_datum;
0099 end
0100
0101 xy_oex = [pos_oex(:,2) pos_oex(:,1)];
0102
0103 % Dynamics_data.m -> OEX depth, heading and corresponding milliseconds timestamps
0104
0105 auv_dyn = Dynamics_data;
0106 AuvDynTime = auv_dyn.TimeStamp.time_t+delay;
0107
0108 temp3 = abs(AuvDynTime - start_run_ms);
0109 [val ind3] = min(temp3);
0110 temp4 = abs(AuvDynTime - end_run_ms);
0111 [val ind4] = min(temp4);
0112 auv_dyn_time_ms = AuvDynTime(ind3:ind4,1);
0113
0114 oex_depth = - auv_dyn.AuvDepth.depth.m(ind3:ind4,1);
0115 oex_heading = auv_dyn.auvHeading.deg(ind3:ind4,1);
0116
0117 waveguide_depth = auv_dyn.AuvAlt.altitude.m(ind3:ind4,1)+abs(oex_depth);
0118
0119
0120 % ========================================================================
0121 % DEPTH OF THE LUBELL SOURCE DURING THE RUN
0122
0123 % from source_logs_20080125.pdf + corresponding text files
0124
0125 timeZero=datenum('00:00:00');
0126 fid=fopen('depthLog_02.txt','r');
0127 c=textscan(fid,'%s > %f');
0128 fclose(fid);
0129 time_depth_log = (24.*(datenum(c{1,1})-timeZero))*60*60*1000;
0130 depth_lubell = -100.*c{1,2};
0131
0132
0133 % ========================================================================
0134 % POSITION OF ROCK AND TARGET (lat/long and localgrid)
0135
0136 target_latlong = [44+(0.8649/60) 9+(49.2638/60)];
```

```
0137 xy_target=[fliplr(geo2utm(target_latlong(1,:),prime_meridian)-utm_datum) -28];
0138
0139 rock_latlong = [44+(0.893/60) 9+(49.2646/60)];
0140 xy_rock= [fliplr(geo2utm(rock_latlong(1,:),prime_meridian)-utm_datum) -27.9];
0141
0142
0143 % ========================================================================
0144 % POSITION OF OTHER FEATURES OF INTEREST (OPTIONAL)
0145
0146 gps_surface = '131335';
0147 gps_surface_ms = (str2num(gps_surface(1:2))*60*60*1000)+ ...
0148     (str2num(gps_surface(3:4))*60*1000)+(str2num(gps_surface(5:6))*1000);
0149
0150 temp8 = abs(AuvPos.TimeStamp.time_t - gps_surface_ms);
0151 [val ind8] = min(temp8);
0152
0153 oex_ll_GPS1 = [AuvPos.AuvPosition.latm.min(ind8,1) ...
0154                AuvPos.AuvPosition.longm.min(ind8,1)]/60;
0155
0156 oex_xy_GPS1  = geo2utm(oex_ll_GPS1(1,:),prime_meridian)-utm_datum;
0157
0158 gps_surface = '125117';
0159 gps_surface_ms = (str2num(gps_surface(1:2))*60*60*1000)+...
0160     (str2num(gps_surface(3:4))*60*1000)+(str2num(gps_surface(5:6))*1000);
0161
0162 temp9 = abs(AuvPos.TimeStamp.time_t - gps_surface_ms);
0163 [val ind9] = min(temp9);
0164
0165 oex_ll_125117 = [AuvPos.AuvPosition.latm.min(ind9,1) ...
0166                  AuvPos.AuvPosition.longm.min(ind9,1)]/60;
0167 oex_xy_125117  = geo2utm(oex_ll_125117(1,:),prime_meridian)-utm_datum;
0168
0169 xy_125117_ll = [44+(0.888/60) 9+(49.265/60)];
0170 xy_125117 = [fliplr(geo2utm(xy_125117_ll(1,:),prime_meridian)-utm_datum)];
0171
0172 time_end = '131335';
0173 time_end_ms = (str2num(time_end(1:2))*60*60*1000) + ...
0174              (str2num(time_end(3:4))*60*1000)+(str2num(time_end(5:6))*1000);
0175
0176
0177 temp10 = abs(AuvPos.TimeStamp.time_t - time_end_ms);
0178 [val ind10] = min(temp10);
0179 oex_final = [AuvPos.AuvPosition.latm.min(ind10,1) ...
0180              AuvPos.AuvPosition.longm.min(ind10,1)]/60;
0181 xy_oex_final  = [fliplr(geo2utm(oex_final(1,:),prime_meridian)-utm_datum)];
0182
0183
0184 % ========================================================================
0185 % PLOT OEX AND LEONARDO PATHS + TARGET LOCATIONS
0186
0187 if 1
0188     figure
0189     plot(xy_oex(:,1),xy_oex(:,2),'k');
0190     hold on
0191     plot(xy_leo(:,1),xy_leo(:,2),'r');
0192     hold on
0193     plot(xy_target(1,1),xy_target(1,2),'ko');
0194     hold on;
0195     plot(xy_rock(1,1),xy_rock(1,2),'ro');
0196     hold on
0197 end
0198 grid on
0199 xlabel('X (m)');
0200 ylabel('Y (m)');
0201 title('Location of OEX and Leonardo during between 12:53:26 and 13:03:26');
0202 legend('OEX path','Leonardo path','elastic target','rock');
0203
0204
```

```
0205 % ========================================================================
0206 % ARRIVAL TIME OF TARGET AND MULTIPATH ECHOES FOR THE SLITA FILES OF THE RUN
0207
0208 if 1
0209
0210     % timestamp of the slita files
0211
0212     f1  = [125402:4:125458];f2 = [125502:4:125558];f3 = [125602:4:125658];
0213     f4  = [125702:4:125758];f5 = [125802:4:125858];f6 = [125902:4:125958];
0214     f7  = [130002:4:130058];f8 = [130102:4:130158];f9 = [130202:4:130258];
0215     f10 = [130302:4:130358];
0216
0217     files_timestamp = [f1 f2 f3 f4 f5 f6 f7 f8 f9 f10 130402];
0218
0219     % file tag is used to specify the index of a timestamp and extract
0220     % corresponding locations of the OEX and Leonardo
0221
0222     file_tag = 100;
0223
0224     for k1=1:length(files_timestamp)
0225
0226         A = floor(files_timestamp(1,k1)/10000);
0227         B = floor((files_timestamp(1,k1) - A*10000)/100);
0228         C = files_timestamp(1,k1) - A*10000 - B*100;
0229
0230         time_file = A*60*60*1000 + B*60*1000 + C*1000 - clock_dif*1000;
0231
0232         % extracts OEX and Leonardo locations associated with timestamp
0233
0234         temp3 = abs(oex_time_ms - time_file);
0235         [val ind3] = min(temp3);
0236
0237         temp4 = abs(leo_time_ms - time_file);
0238         [val ind4] = min(temp4);
0239
0240         % extracts heading of Leonardo associated with timestamp
0241
0242         xy_leo_f = [xy_leo(ind4,:) 0];
0243         if (ind4 > 10)
0244             leo_head_f = mean(leo_head(ind4-10:ind4,1));
0245         else
0246             leo_head_f =leo_head(ind4,1);
0247         end
0248
0249         % depth of Lubell source associated with timestamp
0250
0251         temp5 = abs(time_depth_log - time_file);
0252         [val ind5] = min(temp5);
0253         source_depth_f = depth_lubell(ind5,1);
0254
0255         temp6 = abs(auv_dyn_time_ms - time_file);
0256         [val ind6] = min(temp6);
0257         xy_oex_f = [xy_oex(ind3,:) oex_depth(ind6,1)];
0258         oex_head_f = oex_heading(ind6,1);
0259         H = waveguide_depth(ind6,1);
0260
0261         %~~~~~~~~~~~~~~~~~~~~~~~~~~~~~~~~~~~~~~~~~~~~~~~~~~~~~~~~~~~~~~~~~~~~
0262         % position of the Lubell source relative to the center point Leonardo
0263
0264         dist_mast_frame = 15.5;
0265         frame_length = 5.14;
0266
0267         zs0 = 10.8;             % depth of the source before the ship moves
0268         dist_Aframe_water = 8;
0269
0270         compens = dist_mast_frame + (frame_length/sqrt(2)) + ...
0271             sqrt((zs0+dist_Aframe_water)^2 - ...
0272             (dist_Aframe_water+abs(source_depth_f))^2);
```

```
0273
0274        %~~~~~~~~~~~~~~~~~~~~~~~~~~~~~~~~~~~~~~~~~~~~~~~~~~~~~~~~~~~~~~~~~~~~
0275        % location of the source in localgrid coordinates
0276
0277        xy_source_f(k1,:) = [xy_leo_f(1,1) - ...
0278            compens*sin(leo_head_f*pi/180) xy_leo_f(1,2)- ...
0279            compens*cos(leo_head_f*pi/180) source_depth_f];
0280
0281        L1 = 71.3;
0282
0283        straight_array = 1; % if 1 assumes straight array
0284
0285        %~~~~~~~~~~~~~~~~~~~~~~~~~~~~~~~~~~~~~~~~~~~~~~~~~~~~~~~~~~~~~~~~~~~~
0286        % location of the 1st receiver of the array in localgrid coord
0287
0288        if (straight_array)
0289            xy_rec_f(k1,:)    = [xy_oex_f(1,1)-L1*sin(oex_head_f*pi/180) ...
0290            xy_oex_f(1,2)-L1*cos(oex_head_f*pi/180) oex_depth(ind6,1)]+ ...
0291            [2.74 -34 0];
0292            % note [2.74 -34 0 ] -> navigation error correction
0293        else
0294            % estimation based on array dynamics model
0295            B = load('rec1.mat');
0296            C = load('time_rec.mat');
0297            temp7 = abs(C.time_rec+delay - time_file);
0298            [val ind7] = min(temp7);
0299            temp20 = abs(oex_time_ms - time_file - 56*1000);
0300            [val ind20] = min(temp20);
0301            xy_rec_f(k1,:) = [B.rec1(ind7,:) oex_depth(ind6,1)] + [2.74 -34 0];
0302            % note [2.74 -34 0 ] -> navigation error correction
0303        end
0304
0305        if k1== file_tag
0306            xy_rec_tag = xy_rec_f(k1,:);
0307            xy_src_tag = xy_source_f(k1,:) -[0 10 0];
0308        end
0309
0310        d2_dist_sc_rec(1,k1) = norm(xy_source_f(k1,1:2)-xy_rec_f(k1,1:2),'fro');
0311        d3_dist_sc_rec(1,k1) = norm(xy_source_f(k1,1:3)-xy_rec_f(k1,1:3),'fro');
0312
0313        temp_oex = [xy_oex(ind3,:) -16];
0314        dist_source_oex_rec = norm(xy_source_f(k1,:) - temp_oex,'fro')+ ...
0315            norm(temp_oex- xy_rec_f(k1,:),'fro');
0316
0317        %~~~~~~~~~~~~~~~~~~~~~~~~~~~~~~~~~~~~~~~~~~~~~~~~~~~~~~~~~~~~~~~~~~~~
0318        % computes multipath distance between source and 1st receivers
0319
0320        dir_path(1,k1) = d3_dist_sc_rec(1,k1);
0321
0322        % surface reflected path
0323        srf_path(1,k1)=sqrt((abs(xy_rec_f(k1,3))+abs(source_depth_f))^2+...
0324                        + d2_dist_sc_rec(1,k1)^2);
0325
0326        % bottom reflected path
0327        bot_path(1,k1)=sqrt((-abs(xy_rec_f(k1,3))-abs(source_depth_f)+2*H)^2+...
0328                        + d2_dist_sc_rec(1,k1)^2);
0329
0330        % bottom surface reflected path
0331        bot_srf_path(1,k1) = (sqrt((abs(xy_rec_f(k1,3)) + 2*H - ...
0332            abs(source_depth_f))^2 + d2_dist_sc_rec(1,k1)^2));
0333
0334        % surface bottom reflected path
0335        srf_bot_path(1,k1) = (sqrt((-abs(xy_rec_f(k1,3))+ 2*H + ...
0336            abs(source_depth_f))^2 + d2_dist_sc_rec(1,k1)^2));
0337
0338        % surface bottom surface reflected path
0339        srf_bot_srf_path(1,k1) = (sqrt((abs(xy_rec_f(k1,3))+ 2*H + ...
0340            abs(source_depth_f))^2 + d2_dist_sc_rec(1,k1)^2));
```

```
0341
0342        %  bottom surface surface reflected path
0343        bot_srf_bot_path(1,k1) = (sqrt((-abs(xy_rec_f(k1,3))+ 4*H - ...
0344            abs(source_depth_f))^2 + d2_dist_sc_rec(1,k1)^2));
0345
0346        %~~~~~~~~~~~~~~~~~~~~~~~~~~~~~~~~~~~~~~~~~~~~~~~~~~~~~~~~~~~~~~~~~~~~
0347        % computes target reflected path between source and 1st receivers
0348
0349        target_path(1,k1) = norm(xy_source_f(k1,:) - xy_target,'fro') + ...
0350                            norm(xy_rec_f(k1,:) - xy_target,'fro');
0351
0352        rock_path(1,k1) = norm(xy_source_f(k1,:) - xy_rock,'fro') + ...
0353                          norm(xy_rec_f(k1,:) - xy_rock,'fro');
0354
0355        leo_rec(1,k1) = norm(xy_leo_f(1,:)-xy_rec_f(k1,:),'fro');
0356        src_tgt(1,k1) =  norm(xy_source_f(k1,:) - xy_target,'fro');
0357        tgt_rec(1,k1) =  norm(xy_rec_f(k1,:) - xy_target,'fro');
0358
0359    end
0360
0361    % plots location of 1st receiver/ Lubell source during the run
0362
0363    if 0
0364    hold on
0365    plot(xy_rec_f(:,1),xy_rec_f(:,2),'g');
0366    hold on
0367    plot(xy_source_f(:,1),xy_source_f(:,2),'m');
0368    hold on
0369    end
0370
0371    %=========================================================================
0372    % PLOT OF MULTIPATH AND TARGET REFLECTED ARRIVALS
0373
0374    c0 =1500;       % waveguide sound speed
0375    fs = 51000;     % sampling rate
0376    dt = 1/fs;      % sampling period
0377
0378    % sets the sample at which the direct arrival  is aligned on the plot
0379
0380    time_direct_arrival = 360;
0381
0382    figure
0383    pr = linspace(0,2432,151);
0384    plot(time_direct_arrival*ones(1,151),pr,'r');
0385    hold on
0386    plot(((target_path-dir_path)/(c0*dt))+time_direct_arrival,pr,'k');
0387    hold on
0388    plot(((rock_path-dir_path)/(c0*dt))+time_direct_arrival,pr,'m');
0389    hold on
0390    plot(((srf_path-dir_path)/(c0*dt))+time_direct_arrival,pr);
0391    hold on
0392    plot(((bot_path-dir_path)/(c0*dt))+time_direct_arrival,pr);
0393    hold on
0394    plot(((bot_srf_path-dir_path)/(c0*dt))+time_direct_arrival,pr);
0395    hold  on
0396    plot(((srf_bot_path-dir_path)/(c0*dt))+time_direct_arrival,pr);
0397    hold on
0398    plot(((srf_bot_srf_path-dir_path)/(c0*dt))+time_direct_arrival,pr);
0399    hold on
0400    plot(((bot_srf_bot_path-dir_path)/(c0*dt))+time_direct_arrival,pr);
0401    hold on
0402    axis ij;
0403    axis([0 12000 0 2432]);grid on
0404    legend('direct arrival','target arrival','rock arrival','multipath arrivals');
0405    xlabel('Time (sample)');
0406    ylabel('Ping #');
0407    title('Arrival time of target and multipath echoes during the run');
0408 end
```

A.2 Construction of the TRO -Singular values analysis

The following code is used to process the SLITA files and construct the TR operator for a sliding time window. It produces a set of figures that depict the evolution in time of the first singular values of the TR operator. The time signals of each hydrophone contained in the SLITA files are first extracted using the function `slita_open` provided by M.Mazzi (line 34). The time series are stored in the variable *data_volts_1*. The signal from each hydrophone is then convolved with the impulse response of a Butterworth lowpass filter with cuttoff frequency of 12kHz (line 58). The resulting fitered signals are stored in the variable *filt_signal* and the time serie of the first hydrophone is used as a reference to decompose each signals into pings (line 68). The time window of ping duration is Fourier transformed (line 136) and the complex pressures measured by the receivers are used to construct the TR operator at each frequency (stored in the variable KKH in the code below) using the covariance matrix approach (Eq. 4.1) (line 150). The Singular Value Decomposition of the TR operator (line 164) allows finally to extract its eigenstates. Its singular values and singular vectors are store at each frequency to be transmitted with the virtual TR mirror (line 177).

```
0001 %--------------------------------------------------------------------------
0002 %             CCLNet08 processing -  Singular Value Analysis
0003 %--------------------------------------------------------------------------
0004
0005
0006 %==========================================================================
0007 % SLITA FILE TIMESTAMPS
0008
0009 clear all;
0010
0011 % SLITA files timestamps
0012
0013 f1  = [125402:4:125458];f2 = [125502:4:125558];f3 = [125602:4:125658];
0014 f4  = [125702:4:125758];f5 = [125802:4:125858];f6 = [125902:4:125958];
0015 f7  = [130002:4:130058];f8 = [130102:4:130158];f9 = [130202:4:130258];
0016 f10 = [130302:4:130358];
0017
0018 files_timestamp = [f1 f2 f3 f4 f5 f6 f7 f8 f9 f10 130402];
0019
0020 ww = 100         % index of the file to process
0021
0022 %==========================================================================
0023 % OPENS SELECTED SLITA FILE + LOADS HYDROPHONE TIME SERIES
0024
0025 files = ['sliva_files/sliva_2008025' num2str(files_timestamp(1,ww)); ...
0026          'sliva_files/sliva_2008025' num2str(files_timestamp(1,ww+1))];
0027
0028 [A1 B1]= size(files);
```

```
0029
0030 data_volts_1 = zeros(32,A1*204000);
0031
0032 for k1=1:A1
0033     filename = [files(k1,:) '.dat']
0034     [data_volts, fs, octave, hydrophone_spacing] = slita_open(filename);
0035     temp1 = length(data_volts);
0036     for k2= 1:32
0037         data_volts_1(k2,(k1-1)*temp1+1:k1*temp1) =  data_volts(k2,:);
0038     end
0039 end
0040 clear temp1;
0041
0042 %=========================================================================
0043 % SIGNAL LOW PASS FILTERING
0044
0045 fh = 12000;                 % cuttoff frequency of lowpass filter
0046
0047 [B2 A2] = butter(10,fh/(fs/2),'low');
0048 [H2 T2] = impz(B2,A2,100,fs);
0049
0050 dt = 1/fs;                  % time increment between sample (s)
0051 p_rate = 4;                 % ping rate (Hz)
0052 ns = (1/p_rate)/dt;         % number of samples per ping
0053 nping = 16;                 % number of ping per file
0054
0055 filt_signal = zeros(32,length(data_volts_1));
0056
0057 for k1 = 1:32
0058     temp1                   = conv(H2,data_volts_1(k1,:));
0059     filt_signal(k1,:)       = temp1(1,1:length(data_volts_1));
0060 end
0061 clear temp1;
0062
0063 %=========================================================================
0064 % DETECTION OF DIRECT ARRIVAL + SPLITTING OF TIME SERIES INTO PINGS
0065
0066 % match filtering of hydrophone times series with a sample direct arrival
0067
0068 [mm nn] = find((filt_signal(1,1:ns))==min(((filt_signal(1,1:ns)))));
0069 pulse = filt_signal(1,nn-min(nn,25)+1:nn+25);
0070 cor_pulse(1,:) = conv(filt_signal(1,:),fliplr(pulse));
0071
0072 for k1 = 1:nping
0073     [temp1 temp2] = find(cor_pulse(1,(k1-1)*ns+1:k1*ns) == ...
0074                     max(cor_pulse(1,(k1-1)*ns+1:k1*ns)));
0075     max_cor(1,k1) = temp2;
0076     break_beg(1,k1) = (k1-1)*ns+1+temp2-400;
0077     break_end(1,k1) = k1*ns+1+temp2-400;
0078 end
0079 clear temp1 temp2;
0080
0081
0082 for k1 =1:32
0083     for k2 = 1:nping
0084         data(k2,:,k1) = filt_signal(k1,break_beg(1,k2):break_end(1,k2));
0085     end
0086 end
0087
0088 f1 = 500;
0089 [B2 A2] = butter(10,f1/(fs/2),'high');
0090 [H2 T2] = impz(B2,A2,100,fs);
0091
0092 for k1 = 1:32
0093     for k2 = 1:nping
0094         temp1 = conv(H2,data(k2,:,k1));
0095         data(k2,:,k1) = temp1(1,1:length(data(k2,:,k1)));
0096     end
```

```
0097 end
0098 clear temp1;
0099
0100
0101 %=========================================================================
0102 % TIME WINDOWING + CONSTRUCTION OF TIME REVERSAL OPERATOR
0103
0104 win_start = 2600;
0105 beg_win = win_start;              % time window starting sample
0106 win_duration = 200;             % time window duratio
0107 win_overlap  = 0.75              % overlaping (0.6  -> 60%)
0108
0109 for k1=1:15
0110
0111     beg_win = beg_win + win_duration*(1-win_overlap);
0112     end_win = beg_win + win_duration;
0113
0114     han_win = hanning(200);
0115
0116     % hanning window applied to the time windowed signal
0117
0118     for k2 = 1:nping
0119         for k3 =1:32
0120             data_f(k2,:,k3) = [data(k2,beg_win-100:beg_win-1,k3).*han_win(1:100)' ...
0121                                data(k2,beg_win:end_win,k3) ...
0122      data(k2,end_win+1:end_win+100,k3).*han_win(101:200)'];
0123         end
0124     end
0125
0126     spec_echo = [zeros(nping,1000,32) data_f zeros(nping,10000,32)];
0127
0128     clear ft_spec_echo;
0129     clear A;
0130
0131     for k2 = 1:nping
0132         for k3 =1:32
0133             temp1 = spec_echo(k2,:,k3);
0134             temp2 = length(temp1);
0135             f = (1/dt)*((0:temp2/2-1)/temp2);
0136             ft_spec_echo(k2,:,k3) = (2/temp2)*fft(temp1,temp2);
0137         end
0138     end
0139     clear temp1 temp2;
0140
0141     for k2 =1:1200
0142
0143         % Contruction of the TRO based covariance matrix approach
0144
0145         if 1
0146             % assuming receivers overlap at each emission
0147             KKH=zeros(16,16);
0148             for k3=1:16
0149                 P(:,k3) = ft_spec_echo(k3,k2,k3:k3+15);
0150                 KKH = KKH+P(:,k3)*P(:,k3)';
0151             end
0152         else
0153             % assuming receivers overlap at every other emission
0154             KKH=zeros(8,8);
0155             for k3=1:8
0156                 P(:,k3) = ft_spec_echo((k3*2)-1,k2,(k3-1)*3+1:(k3-1)*3+1+7);
0157                 KKH = KKH+P(:,k3)*P(:,k3)';
0158             end
0159         end
0160
0161         [eig_vec,eig_val] = eig(KKH);
0162         eig_TRO(k2,:) = sum(eig_val);
0163
0164         [U,S,V] = svd(KKH);
```

```
0165          sing_val(k2,:)=sum(S);
0166          sum_sing(1,k2) = sum(sum(S));
0167
0168
0169          eig_vec_1(:,k2) = eig_vec(:,1);
0170          eig_vec_2(:,k2) = eig_vec(:,2);
0171          eig_vec_3(:,k2) = eig_vec(:,3);
0172          eig_vec_4(:,k2) = eig_vec(:,4);
0173          eig_vec_5(:,k2) = eig_vec(:,5);
0174
0175      end
0176
0177      store_SV1(:,k1) = sing_val(:,1);
0178      store_SV2(:,k1) = sing_val(:,2);
0179      store_SV3(:,k1) = sing_val(:,3);
0180      store_SV4(:,k1) = sing_val(:,4);
0181
0182  end
0183
0184
0185  XX = [win_start:50:end_win];
0186  YY = fliplr(f(1,1:1200));
0187
0188  figure;imagesc(XX,YY,flipud(store_SV1));
0189  title('SV1');
0190  xlabel('Time (sample)');
0191  ylabel('Frequency (Hz)');
0192
0193  figure;imagesc(XX,YY,flipud(store_SV2));
0194  title('SV2');
0195  xlabel('Time (sample)');
0196  ylabel('Frequency (Hz)');
0197
0198  figure;imagesc(XX,YY,flipud(store_SV3));
0199  title('SV3');
0200  xlabel('Time (sample)');
0201  ylabel('Frequency (Hz)');
0202
0203  figure;imagesc(XX,YY,flipud(store_SV4));
0204  title('SV4');
0205  xlabel('Time (sample)');
0206  ylabel('Frequency (Hz)');
0207
0208
0209
0210  save target_ping1520_eig_vec eig_vec_1 eig_vec_2 eig_vec_3;
```

A.3 Backpropagation of eigenvectors

The following code is used to backpropagate on the seabed the singular vectors of the TR operator (see section A.2). It produces a set of top view plots of the pressure field on the seabed (see Fig. 4.17(b). The backpropagation can either be conducted in a free field environement or in a waveguide using precomputed green functions (line 91).

```
0001 %--------------------------------------------------------------------------
0002 %                  CCLNet08 - BACKPROPAGATION OF EIGENVECTORS
0003 %--------------------------------------------------------------------------
0004
0005 clear all;
0006 clc;
0007 warning off;
0008
0009 % ========================================================================
0010 %   Characteristics of the grid
0011
0012 nX = 60;                      % number of grid points in x direction
0013 nY = 60;                      % number of grid points in y direction
0014 nGP =  (2*nX+1)*(2*nY+1);     % total number of grid points
0015 step_x = 1e-3                 % step increment in x direction (km)
0016 step_y = 1e-3                 % step increment in y direction (km)
0017
0018 % grid point coordinates
0019
0020 [grid_x grid_y] = meshgrid(-nX*step_x:step_x:nX*step_x,-nY*step_y:step_y:nY*step_y);
0021
0022 % ========================================================================
0023 %  Characteristics of the array + hydrophone coordinates
0024
0025 freq = 1000;          % frequency of backpropagation
0026
0027 nR = 16;              % number of receivers considered for the backpropagation
0028 dRR = 0.211;          % distance between the receivers of the array (m)
0029 dpth_R = 16;          % depth of the receivers (m)
0030
0031 % sets the receivers (i.e sources) coordinates
0032
0033 hyd_x = [0:dRR:(nR-1)*dRR]/1e3;
0034 p_r(:,1) = hyd_x';
0035 p_r(:,2) = zeros(1,16)';
0036 p_r(:,3) = dpth_R*ones(1,16)/1e3';
0037
0038 % Note: defines a horizontal array pointing in the +x direction
0039
0040 % ========================================================================
0041 %  Distance receivers - grid points
0042
0043 dRGP     = zeros(nR,nGP);
0044 temp_RGP =  NaN*ones(2*nX+1,2*nY+1);
0045
0046 for k1=1:nR
0047     temp_RGP = sqrt((grid_x - p_r(k1,1)).^2 + (grid_y - p_r(k1,2)).^2);
0048     dRGP(k1,:) = reshape(temp_RGP',1,nGP);
0049 end
0050
0051
0052
0053
```

```
0054 % ==========================================================================
0055 %  Load  eigenvectors to backpropagate
0056
0057 temp1 = load('target_ping1450_eig_vec.mat');
0058
0059 df = 4.5532;
0060 vec_tag = floor(freq/df);
0061 T = temp1.eig_vec_3(:,vec_tag);
0062
0063 temp2 = T ;
0064
0065 % ==========================================================================
0066 %  Backpropagation in free field or using precomputed green functions
0067
0068 gp_mag  = NaN*ones(1,nGP);
0069 gp_phase= NaN*ones(1,nGP);
0070
0071 C = NaN*ones(nR,nGP);
0072 dist3D = zeros(nGP,1);
0073
0074 c0 = 1500;          % sound speed in water
0075 DP = 30;            % depth of waveguide
0076
0077 free_field = 1
0078
0079 if (free_field)
0080     for k1=1:nR
0081         k1
0082         dist3D = sqrt((1000*dRGP(k1,:)').^2+(DP-dpth_R).^2);
0083         green_func = exp(-j*(2*pi*freq/c0)*dist3D)./dist3D;
0084         gp_mag    = temp2(k1)*abs(green_func);
0085         gp_phase  = phase(green_func);
0086         C(k1,:)   = gp_mag.*exp(j*gp_phase);
0087         dist3D = zeros(nGP,1);
0088     end
0089 else
0090     for k1=1:nR
0091         filename = ['CCLNET08_' num2str(freq) '_0_0.3_' num2str(dpth_R) '.mat'];
0092         A=load(filename);
0093         mag_T   = abs(A.T);
0094         phase_T = phase(A.T);
0095         gp_mag    = temp2(k1)*interp1q(A.range', mag_T',dRGP(k1,:)');
0096         gp_phase  = interp1q(A.range', phase_T',dRGP(k1,:)');
0097         C(k1,:)   = gp_mag.*exp(j*gp_phase);
0098     end
0099 end
0100
0101
0102 % ==========================================================================
0103 %  Computes pressure amplitude at each grid point location.
0104
0105 pres_GP = abs(sum(C));
0106
0107 Z = zeros(2*nX+1,2*nY+1,1);
0108
0109 k=0;
0110 for k1=1:2*nY+1
0111     for k2=1:2*nX+1
0112         k = k+1;
0113         Z(k1,k2)=pres_GP(k);
0114     end
0115 end
0116
0117 % ==========================================================================
0118 %  Plots pressure field on the seabed
0119
0120 X = [-nX*step_x:step_x:nX*step_x]*1e3;
0121 Y = [-nY*step_y:step_y:nY*step_y]*1e3;
```

```
0122
0123 figure
0124 imagesc(X,Y,Z);
0125 cmap_smooth = jet(500);
0126 colormap(cmap_smooth);
0127
0128 xlabel('X (m)');
0129 ylabel('Y (m)');
0130 mes_title = ['freq = ' num2str(freq)];
0131 title(mes_title);
0132 colorbar;
0133 hold on
0134 drawnow;
```

Appendix B

SLITA Specifications

The following technical drawing of the SLITA array was provided by Alain Maguer from NURC (NATO Undersea Research Center)

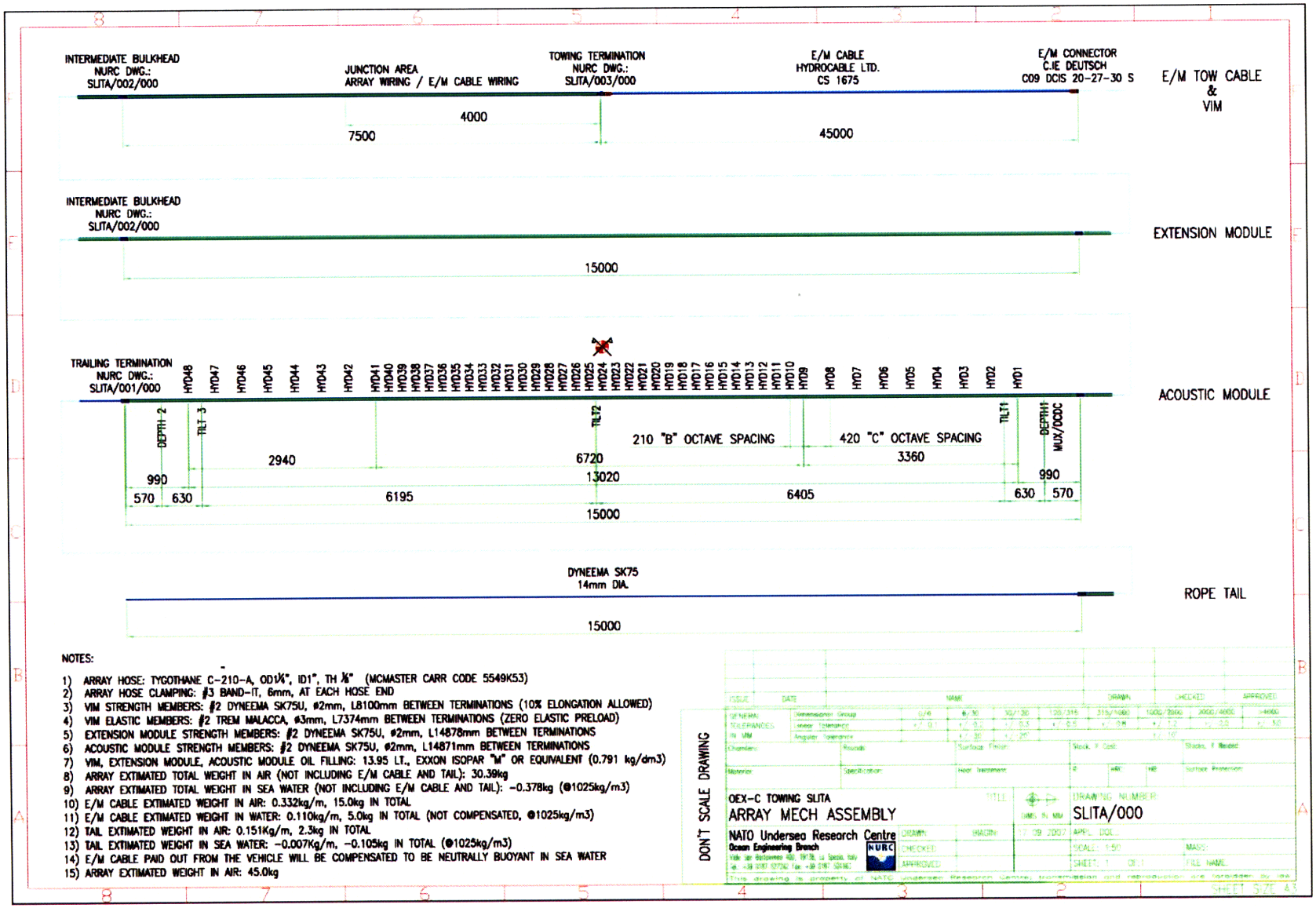

NOTES:

1) ARRAY HOSE: TYGOTHANE C-210-A, OD1¼", ID1", TH ⅛" (MCMASTER CARR CODE 5549K53)
2) ARRAY HOSE CLAMPING: #3 BAND-IT, 6mm, AT EACH HOSE END
3) VIM STRENGTH MEMBERS: #2 DYNEEMA SK75U, ø2mm, L8100mm BETWEEN TERMINATIONS (10% ELONGATION ALLOWED)
4) VIM ELASTIC MEMBERS: #2 TREM MALACCA, ø3mm, L7374mm BETWEEN TERMINATIONS (ZERO ELASTIC PRELOAD)
5) EXTENSION MODULE STRENGTH MEMBERS: #2 DYNEEMA SK75U, ø2mm, L14878mm BETWEEN TERMINATIONS
6) ACOUSTIC MODULE STRENGTH MEMBERS: #2 DYNEEMA SK75U, ø2mm, L14871mm BETWEEN TERMINATIONS
7) VIM, EXTENSION MODULE, ACOUSTIC MODULE OIL FILLING: 13.95 LT., EXXON ISOPAR "M" OR EQUIVALENT (0.791 kg/dm3)
8) ARRAY EXTIMATED TOTAL WEIGHT IN AIR (NOT INCLUDING E/M CABLE AND TAIL): 30.39kg
9) ARRAY EXTIMATED TOTAL WEIGHT IN SEA WATER (NOT INCLUDING E/M CABLE AND TAIL): -0.378kg (@1025kg/m3)
10) E/M CABLE EXTIMATED WEIGHT IN AIR: 0.332kg/m, 15.0kg IN TOTAL
11) E/M CABLE EXTIMATED WEIGHT IN WATER: 0.110kg/m, 5.0kg IN TOTAL (NOT COMPENSATED, @1025kg/m3)
12) TAIL EXTIMATED WEIGHT IN AIR: 0.151Kg/m, 2.3kg IN TOTAL
13) TAIL EXTIMATED WEIGHT IN SEA WATER: -0.007Kg/m, -0.105kg IN TOTAL (@1025kg/m3)
14) E/M CABLE PAID OUT FROM THE VEHICLE WILL BE COMPENSATED TO BE NEUTRALLY BUOYANT IN SEA WATER
15) ARRAY EXTIMATED WEIGHT IN AIR: 45.0kg

DON'T SCALE DRAWING

OEX-C TOWING SLITA
ARRAY MECH ASSEMBLY

NATO Undersea Research Centre
Ocean Engineering Branch

DRAWING NUMBER
SLITA/000

Bibliography

[1] A. Tesei, A. Maguer, WLJ Fox, R. Lim, and H. Schmidt. Measurements and modeling of acoustic scattering from partially and completely buried spherical shells. *The Journal of the Acoustical Society of America*, 112:1817, 2002.

[2] D. Ghosh. Experimental and Modeling Analysis of Near-field Scattering from Complex Targets, 2008.

[3] I. Lucifredi and H. Schmidt. Subcritical scattering from buried elastic shells. *The Journal of the Acoustical Society of America*, 120:3566, 2006.

[4] Mario Zampolli, Alessandra Tesei, Finn B. Jensen, Nils Malm, John B. Blottman, and III. A computationally efficient finite element model with perfectly matched layers applied to scattering from axially symmetric objects. *The Journal of the Acoustical Society of America*, 122(3):1472–1485, 2007.

[5] H. Schmidt and G. Tango. Efficient global matrix approach to the computation of synthetic seismograms. *Geophysical Journal International*, 84(2):331–359, 1986.

[6] M.R. Benjamin, D. Battle, D. Eickstedt, H. Schmidt, and A. Balasuriya. Autonomous Control of an Autonomous Underwater Vehicle Towing a Vector Sensor Array. *Robotics and Automation, 2007 IEEE International Conference on*, pages 4562–4569, 2007.

[7] C. Prada, S. Manneville, D. Spoliansky, and M. Fink. Decomposition of the time reversal operator: Detection and selective focusing on two scatterers. *The Journal of the Acoustical Society of America*, 99:2067, 1996.

[8] C. Prada, M. Tanter, and M. Fink. Flaw detection in solid with the DORT method. *Ultrasonics Symposium, 1997. Proceedings., 1997 IEEE*, 1, 1997.

[9] N. Mordant, C. Prada, and M. Fink. Highly resolved detection and selective focusing in a waveguide using the DORT method. *The Journal of the Acoustical Society of America*, 105:2634, 1999.

[10] C. Prada and J.L. Thomas. Experimental subwavelength localization of scatterers by decomposition of the time reversal operator interpreted as a covariance matrix. *The Journal of the Acoustical Society of America*, 114:235, 2003.

[11] C. Prada and M. Fink. Eigenmodes of the time reversal operator: a solution to selective focusing in multiple-target media. *Wave motion*, 20(2):151–163, 1994.

[12] C. Prada, J.L. Thomas, and M. Fink. The iterative time reversal process: Analysis of the convergence. *The Journal of the Acoustical Society of America*, 97:62, 1995.

[13] D.H. Chambers and AK Gautesen. Time reversal for a single spherical scatterer. *The Journal of the Acoustical Society of America*, 109:2616, 2001.

[14] JF Lingevitch, HC Song, and WA Kuperman. Time reversed reverberation focusing in a waveguide. *The Journal of the Acoustical Society of America*, 111:2609, 2002.

[15] G.F. Edelmann, J.F. Lingevitch, C.F. Gaumond, D.M. Fromm, and D.C. Calvo. Comparison of a subrank to a full-rank time-reversal operator in a dynamic ocean. *The Journal of the Acoustical Society of America*, 122:2706, 2007.

[16] A. Cantoni and LC Godara. Resolving the directions of sources in a correlated field incident on an array. *The Journal of the Acoustical Society of America*, 67:1247, 1980.

[17] G. Bienvenu and L. Kopp. Optimality of high resolution array processing using the eigensystem approach. *Acoustics, Speech, and Signal Processing [see also IEEE Transactions on Signal Processing], IEEE Transactions on*, 31(5):1235–1248, 1983.

[18] L. Flax and C.M. Davis Jr. Scattering of sound from layered elastic spheres. *The Journal of the Acoustical Society of America*, 55:S83, 1974.

[19] L. Flax, GC Gaunaurd, and H. Uberall. Theory of resonance scattering. *Physical Acoustics*, 15:191–294, 1981.

[20] N.D. Veksler. *Resonance*. Springer-Verlag, 1993.

[21] M. Fink, C. Prada, F. Wu, and D. Cassereau. Self focusing in inhomogeneous media with time reversal acousticmirrors. *Ultrasonics Symposium, 1989. Proceedings., IEEE 1989*, pages 681–686, 1989.

[22] C. Prada, F. Wu, and M. Fink. The iterative time reversal mirror: A solution to self-focusing in the pulse echo mode. *The Journal of the Acoustical Society of America*, 90:1119, 1991.

[23] HC Song, WA Kuperman, WS Hodgkiss, T. Akal, and C. Ferla. Iterative time reversal in the ocean. *The Journal of the Acoustical Society of America*, 105:3176, 1999.

[24] G. Montaldo, M. Tanter, and M. Fink. Revisiting iterative time reversal processing: Application to detection of multiple targets. *The Journal of the Acoustical Society of America*, 115:776, 2004.

[25] G. Montaldo, M. Tanter, and M. Fink. Real time inverse filter focusing through iterative time reversal. *The Journal of the Acoustical Society of America*, 115:768, 2004.

[26] C. Prada, N. Lartillot, and M. Fink. Selective focusing in multiple-target media: the transfer matrixmethod. *Ultrasonics Symposium, 1993. Proceedings., IEEE 1993*, pages 1139–1142.

[27] C. Prada, E. Senbati, M. Fink, and P.V.I.I. CNRS. Decomposition of the time reversal operator: Application to dispersion curve measurements. *Ultrasonics Symposium, 1994. Proceedings., 1994 IEEE*, 2, 1994.

[28] C. Prada and M. Fink. Separation of interfering acoustic scattered signals using the invariants of the time-reversal operator. Application to Lamb waves characterization. *The Journal of the Acoustical Society of America*, 104:801, 1998.

[29] J.G. Minonzio, C. Prada, D. Chambers, D. Clorennec, and M. Fink. Characterization of subwavelength elastic cylinders with the decomposition of the time-reversal operator: Theory and experiment. *The Journal of the Acoustical Society of America*, 117:789, 2005.

[30] DH Chambers. Analysis of the time-reversal operator for scatterers of finite size. *The Journal of the Acoustical Society of America*, 112:411, 2002.

[31] J.G. Minonzio, F.D. Philippe, C. Prada, and M. Fink. Time-reversal operator for elastic cylinder and sphere. *Inverse Problems*, 24:025014, 2008.

[32] C. Prada and M. Fink. Selective focusing through inhomogeneous media: the DORT method. *Ultrasonics Symposium, 1995. Proceedings., 1995 IEEE*, 2, 1995.

[33] P. Roux and M. Fink. Time reversal in a waveguide: Study of the temporal and spatial focusing. *The Journal of the Acoustical Society of America*, 107:2418, 2000.

[34] K.G. Sabra, S.R. Khosla, and D.R. Dowling. Broadband time-reversing array retrofocusing in noisy environments. *The Journal of the Acoustical Society of America*, 111:823, 2002.

[35] K.G. Sabra and D.R. Dowling. Broadband performance of a moving time reversing array. *The Journal of the Acoustical Society of America*, 114:1395, 2003.

[36] K.G. Sabra and D.R. Dowling. Effects of time-reversing array deformation in an ocean wave guide. *The Journal of the Acoustical Society of America*, 115:2844, 2004.

[37] K.G. Sabra and D.R. Dowling. Effect of ocean currents on the performance of a time-reversing array in shallow water. *The Journal of the Acoustical Society of America*, 114:3125, 2003.

[38] T. Folegot, C. Prada, and M. Fink. Resolution enhancement and separation of reverberation from target echo with the time reversal operator decomposition. *The Journal of the Acoustical Society of America*, 113:3155, 2003.

[39] S. Kim, WA Kuperman, WS Hodgkiss, HC Song, G. Edelmann, and T. Akal. Echo-to-reverberation enhancement using a time reversal mirror. *The Journal of the Acoustical Society of America*, 115:1525, 2004.

[40] HC Song, S. Kim, WS Hodgkiss, and WA Kuperman. Environmentally adaptive reverberation nulling using a time reversal mirror. *The Journal of the Acoustical Society of America*, 116:762, 2004.

[41] C.F. Gaumond, D.M. Fromm, J.F. Lingevitch, R. Menis, G.F. Edelmann, D.C. Calvo, and E. Kim. Demonstration at sea of the decomposition-of-the-time-reversal-operator technique. *The Journal of the Acoustical Society of America*, 119:976, 2006.

[42] S. Hou, K. Solna, and H. Zhao. Imaging of location and geometry for extended targets using the response matrix. *Journal of Computational Physics*, 199(1):317–338, 2004.

[43] S. Hou, K. Solna, and H. Zhao. A direct imaging method using far-field data. *Inverse Problems*, 23(4):1533–1546, 2007.

[44] L. Carin, H. Liu, T. Yoder, L. Couchman, B. Houston, and J. Bucaro. Wideband time-reversal imaging of an elastic target in an acoustic waveguide. *The Journal of the Acoustical Society of America*, 115:259, 2003.

[45] F.B. Jensen. *Computational Ocean Acoustics*. Amer Inst of Physics, 1994.

[46] H. Schmidt. SAFARI: Seismo-Acoustic Fast Field Algorithm for Range-Independent Environments. User's Guide. 1988.

[47] H. Schmidt and F.B. Jensen. A full wave solution for propagation in multilayered viscoelastic media with application to Gaussian beam reflection at fluid–solid interfaces. *The Journal of the Acoustical Society of America*, 77:813, 1985.

[48] H. Schmidt. OASES Version 3.1 User Guide and Reference Manual. *Department of Ocean Engineering, Massachusetts Institute of Technology*, 2004.

[49] H. Schmidt and J. Glattetre. A fast field model for three-dimensional wave propagation in stratified environments based on the global matrix method. *The Journal of the Acoustical Society of America*, 78:2105, 1985.

[50] A. Maguer, R. Dymond, M. Mazzi, S. Biagini, S. Fioravanti, and P. Guerrini. SLITA: A new slim towed array for AUV applications. *The Journal of the Acoustical Society of America*, 123(5):3005, 2008.

[51] P.M. Newman. MOOS-Mission Orientated Operating Suite. 2001.

[52] Latchman S. Milinazzo F., Wilkie M. Efficient algorithm for simulating the dynamics of towed cable systems. *Ocean Engineering*, 14(6):513–526, 1987.